

Memorization to Generalization: Emergence of Diffusion Models from Associative Memory

Bao Pham^{*1}, Gabriel Raya^{*2}, Matteo Negri³,
Mohammed J. Zaki¹, Luca Ambrogioni⁴, and Dmitry Krotov⁵

¹Department of Computer Science, Rensselaer Polytechnic Institute

²Jheronimus Academy of Data Science, Tilburg University

³Department of Physics, University of Rome Sapienza

⁴Donders Institute, Radboud University

⁵MIT-IBM Watson AI Lab, IBM Research

Abstract

Hopfield networks are associative memory (AM) systems, designed for storing and retrieving patterns as local minima of an energy landscape. In the classical Hopfield model, an interesting phenomenon occurs when the amount of training data reaches its critical memory load — *spurious states*, or unintended stable points, emerge at the end of the retrieval dynamics, leading to incorrect recall. In this work, we examine diffusion models, commonly used in generative modeling, from the perspective of AMs. The training phase of diffusion model is conceptualized as memory encoding (training data is stored in the memory). The generation phase is viewed as an attempt of memory retrieval. In the small data regime the diffusion model exhibits a strong memorization phase, where the network creates distinct basins of attraction around each sample in the training set, akin to the Hopfield model below the critical memory load. In the large data regime, a different phase appears where an increase in the size of the training set fosters the creation of new attractor states that correspond to manifolds of the generated samples. Spurious states appear at the boundary of this transition and correspond to emergent attractor states, which are absent in the training set, but, at the same time, have distinct basins of attraction around them. Our findings provide: a novel perspective on the memorization-generalization phenomenon in diffusion models via the lens of AMs, theoretical prediction of existence of spurious states, empirical validation of this prediction in commonly-used diffusion models.

The code is available at: <https://github.com/Lemon-cmd/Diffusion-Models-and-Associative-Memory>
^{*} denotes equal contribution.

1 Introduction

Hopfield networks are the simplest energy-based models that conceptualize memories as attractor states corresponding to local minima of their energy function, and the memory retrieval as dynamical convergence towards those attractor states [1–3]. Recently, they have seen a resurgence of interest due to advances in their memorization capacity. Notably, Dense Associative Memories (DenseAMs), which are extensions of Hopfield networks with super-linear memory capacity [4,5] have paved the way for more sophisticated associative memory systems [6–18], driven in part by their connection to the attention mechanism in transformers [13,19,20] and to neurobiology [20,21]. Simultaneously, generative diffusion models [22] have gained considerable popularity, due to their flexibility and accuracy in modeling high-dimensional distributions for a variety of domains—such as image generation [23–25], audio [26–28], video synthesis [29–32], and other scientific applications. However, despite their effectiveness, diffusion models pose challenges related to privacy and security, as concerns grow about their tendency to replicate training data [33–35]. Such matters consequently emphasize the need for further understanding of memorization and generalization behaviors in diffusion models.

Recent works [36–38] have begun establishing theoretical connections between DenseAMs and generative diffusion models, offering a foundation for bridging the two fields. Specifically, it was shown that the logarithm of the probability of the generated samples in diffusion models can be interpreted as the energy function of a commonly used DenseAM model with the `softmax` activation function. This makes it possible to apply theoretical tools developed for associative memory to better understand the computational properties of diffusion models.

A possible key that can further bridge these two systems and highlight the properties of the memorization-to-generalization transition in diffusion models is the phenomenon of *spurious patterns*. Historically considered as detrimental to pattern recall [39–41], spurious patterns can be interpreted as combinations or interpolations of stored patterns, hinting at the network’s ability to synthesize new patterns from existing training data. This blending of fundamental memories resembles the generalization process in generative models, where learned representations are used to generate novel outputs. In this way, spurious patterns offer a fascinating framework for exploring the balance between memorization — where models store exact patterns from training data — and generalization, where they use underlying features to create genuinely new samples [42]. Studying the conditions under which spurious patterns emerge and how they contribute to the network’s behavior can thus shed light on generalization in both associative memory and contemporary generative models.

Previous works have explored memorization in generative models through various approaches. For instance, [43,44] proposed general methods to measure memorization, while [33,34,45,46] examined the memorization capacity in diffusion models as a function of the size of the training data. Other works have focused on understanding generalization, such as the theoretical estimates of the generalization gap [47], and the spectral analyses [48–50]. A recent study [51] proposed that generalization in diffusion models arises as a result of the combination of limited capacity and structural constraints neural network, which results in predictable patterns at the boundary between memorization and generalization. Other recent studies [49,50,52] explored memorization

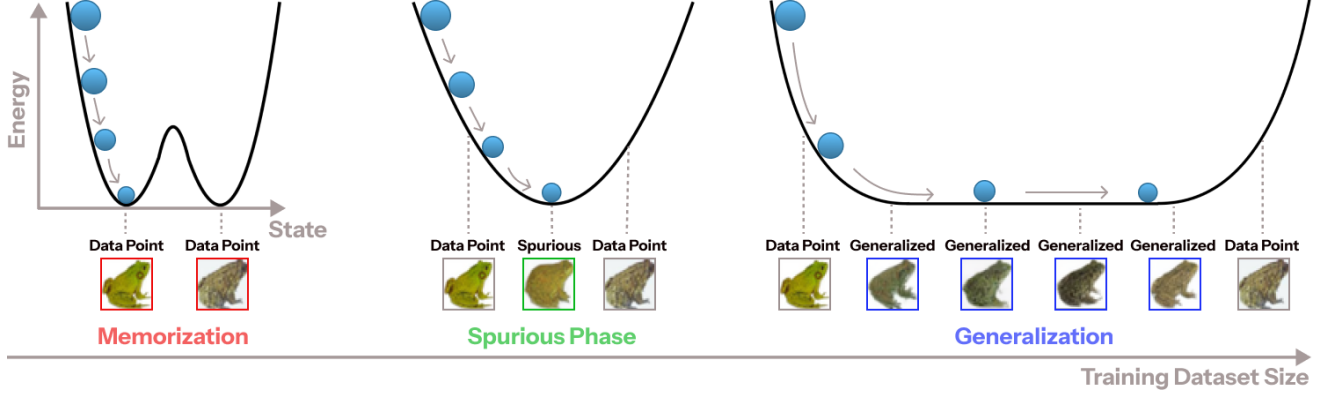


Figure 1: A simple illustration depicting the change in the energy landscape as the size of the training dataset is increased. In the small data regime, the model memorizes the training data points as local minima of the energy. When the amount of training data exceeds the memory capacity of the model, spurious patterns are formed and training data points are no longer energy minima. Subsequent increase of the training set size leads to the generalization phase, which is defined by the formation of continuous manifold of the low energy states.

and generalization through the relationship between the dimensionalities of the ground-truth manifold and the manifold that is learned by the model. Meanwhile, [53] explored the evolution of the generated density as a function of the training time to provide an analysis on how mode collapse occurs and leads to the loss of diversity in the generated density. Finally, [54] and [55] characterized memorization in diffusion models as “condensation” phase transitions known in the statistical physics of spin glasses and random energy models. Although these studies shed some light on memorization and generalization, they do not fully explore the model’s behavior during the transition between these two phases.

Contributions. Most of the mentioned works on memorization-to-generalization transition tackled it in a generalization-centric fashion. Namely, the memorization phenomenon is typically viewed as a “small side effect” of the diffusion models. In our work we adopt a complimentary approach. From the beginning, we cast the diffusion modeling pipeline into the associative memory framework. The training phase of the diffusion model is conceptualized as *writing into the memory* operation. The generation phase is viewed as *an attempt of memory recall*. This recall can be successful, resulting in the retrieval of training samples (memorization), or unsuccessful, resulting in the generation of new previously unseen samples (generalization). Thus, according to this theory, generalization (creation of genuinely novel samples) is a failure of memory recall. This point of view allows us to apply theory developed in DenseAMs for analyzing the memorization-to-generalization transition.

In DenseAMs, it is well-known that successful memory recall deteriorates as the number of the stored data points increases [4]. Importantly, the transition from successful to unsuccessful memory recall is marked by the peculiar phenomenon — the emergence of spurious states, see Fig. (1). Our theory provides a specific and empirically verifiable prediction — spurious states must exist in the conventional diffusion models, which are trained and ran using standard methods.

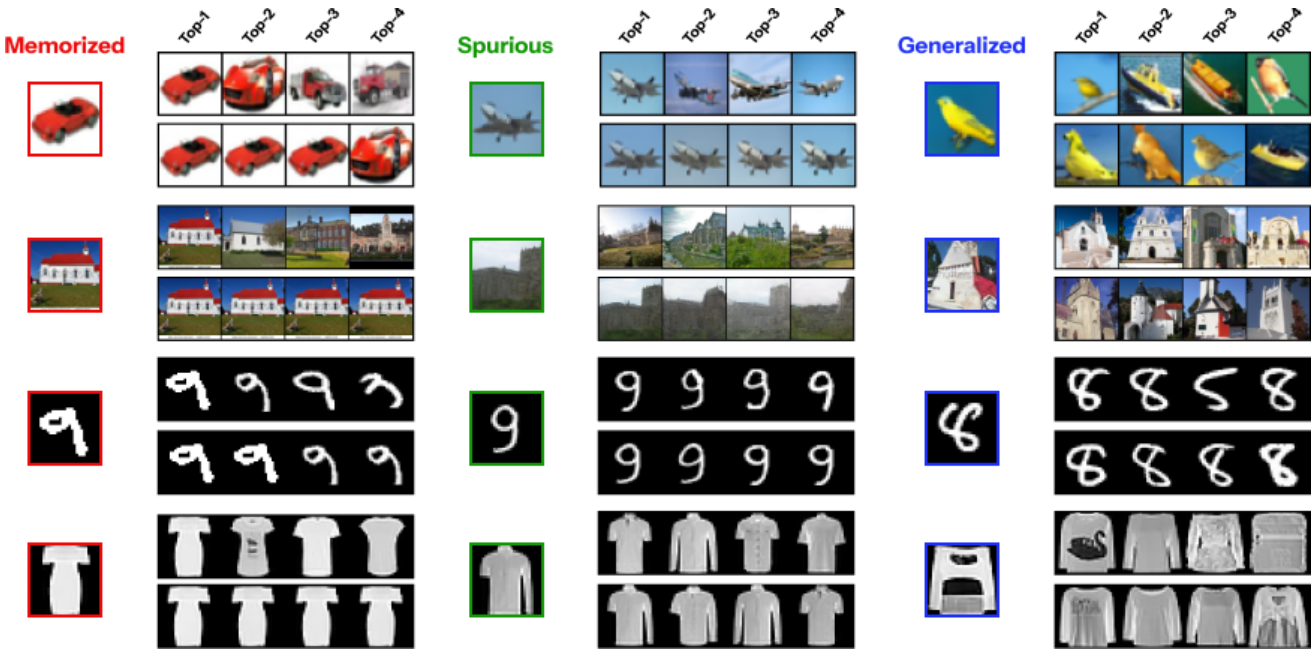


Figure 2: Examples of **memorized**, **spurious**, and **generalized** samples in their respective columns for four datasets. For each target image (shown on the left), its **top-4** nearest neighbors from the training set (**top row**) and the synthetic set (**bottom row**) are shown to highlight the novelty or the commonality of the target image with respect to training and synthetic sets. Memorized samples are duplicates of the training points. Spurious samples are copies of the synthetic set that do not appear in the training set. Generalized samples do not belong to either of the two sets, indicating that they are genuinely novel samples that are not generated frequently.

In this paper we demonstrate that this is indeed the case. Spurious states emerge at the boundary between the memorization and generalization phases, see examples of spurious samples in Fig. (2).

In accord with previous literature, we find that **(1)** diffusion models undergo a transition from memorization to generalization as the number of training points increases; **(2)** unlike previous works on diffusion models, at the onset of generalization we detect the emergence of spurious patterns, which have sizable basins of attraction, but are not memorized data points; and lastly, **(3)** we provide theoretical descriptions distinguishing these spurious states from memorized and generalized patterns in terms of energy landscapes. All of these findings suggest a close parallel between diffusion models and DenseAMs above the critical storage capacity.

2 Diffusion Models and Dense Associative Memories

Given a dataset of i.i.d. samples $\mathbf{y} \in \mathbb{R}^N$ drawn from a target data distribution $p(\mathbf{y})$, diffusion models are a class of generative models, which aims to approximate $p(\mathbf{y})$ by placing a reversible process that maps data to noise and back. The mapping to noise (or forward process) is described by the following Itô Stochastic Differential Equation (SDE) [25]:

$$d\mathbf{x}_t = \mathbf{f}(\mathbf{x}_t, t)dt + g(t)d\mathbf{w}_t \quad (1)$$

which transforms the given data distribution ($\mathbf{x}_0 = \mathbf{y}$) into a simpler one, such as an isotropic Gaussian distribution. Here, \mathbf{w}_t is the standard Wiener process (or Brownian motion) and $\mathbf{f}(\mathbf{x}_t, t)$ denotes the drift term that guides the diffusion process, which we will assume to be zero for the most part of this paper. Meanwhile, $g(t)$ represents the diffusion coefficient that controls the noise at each time step $t \rightarrow T$. The reverse process removes the injected noise and is described as

$$d\mathbf{x}_t = [\mathbf{f}(\mathbf{x}_t, t) - g(t)^2 \nabla_{\mathbf{x}_t} \log p_t(\mathbf{x}_t)] dt + g(t) d\bar{\mathbf{w}}_t \quad (2)$$

where $\bar{\mathbf{w}}_t$ is the standard Wiener process. To effectively solve this equation, one must reliably estimate the score $\nabla_{\mathbf{x}_t} \log p_t(\mathbf{x}_t)$ via parameterization of the score as a neural network $s_\theta(\mathbf{x}, t)$, where θ denotes neural network's trainable parameters. This network is trained using methods for denoising score matching across multiple times steps [23, 25, 56–58].

Our theoretical arguments pertain to the idealistic setting in which this neural network is capable of learning the true empirical distribution obtained by adding noise to the training data. This limiting case is often adopted in theoretical studies of diffusion models, see [54, 55, 59–61]. From the practical perspective, this is achieved if the neural network is large (over-parametrized) and trained for a long time, an assumption that may deviate from the practical use cases. This simplification allows us to make a theoretical prediction that diffusion models must generate spurious states. It is highly non-trivial that this theoretical prediction can be extrapolated to the regime in which the size of the score-modeling neural network is finite and the amount of training data is large. The main contribution of our work is the empirical demonstration that this extrapolation is valid, and spurious states indeed exist in practically used settings.

Consider the training data distribution in the variance-exploding setting of $f(\mathbf{x}_t, t) = 0$ and $g(t) = \sigma$. In this case, the marginal probability distribution of new samples can be computed exactly as

$$p(\mathbf{x}_t, t) = \mathbb{E}_{\mathbf{y} \sim \text{data}} \left[\frac{1}{(2\pi\sigma^2 t)^{\frac{N}{2}}} \exp \left(-\frac{\|\mathbf{x}_t - \mathbf{y}\|_2^2}{2\sigma^2 t} \right) \right] \quad (3)$$

Assuming the empirical distribution of the data $p(\mathbf{y}) = \frac{1}{K} \sum_{\mu=1}^K \delta^{(N)}(\mathbf{y} - \boldsymbol{\xi}^\mu)$, where $\boldsymbol{\xi}^\mu$ represents an individual data point (with data size K), this marginal distribution can be written as

$$p(\mathbf{x}_t, t) = \frac{1}{K} \sum_{\mu=1}^K \frac{1}{(2\pi\sigma^2 t)^{\frac{N}{2}}} \exp \left(-\frac{\|\mathbf{x}_t - \boldsymbol{\xi}^\mu\|_2^2}{2\sigma^2 t} \right) \stackrel{\text{def}}{=} \exp \left(-\frac{E^{\text{DM}}(\mathbf{x}_t, t)}{2\sigma^2 t} \right) \quad (4)$$

where we also defined the energy E^{DM} of diffusion model, which up to state- or \mathbf{x} -independent terms is equal to

$$E^{\text{DM}}(\mathbf{x}_t, t) = -2\sigma^2 t \log \left[\sum_{\mu=1}^K \exp \left(-\frac{\|\mathbf{x}_t - \boldsymbol{\xi}^\mu\|_2^2}{2\sigma^2 t} \right) \right] \quad (5)$$

As already observed in [37], this energy function (5) is closely related to the class of models called DenseAMs, or Modern Hopfield Networks, which are large memory storage variants of classical Hopfield networks [4, 62].

The core idea behind DenseAMs is to design an energy function that sharply peaks around the intended memory patterns. These networks can store and retrieve a much larger number of memories, compared to the classical Hopfield networks, which scales super-linearly (and possibly exponentially) to the size of the network and decouples information storage capacity from the dimensionality of the data [4, 6]. Of particular interest here is the DenseAM model studied in [12] (see also [11]):

$$E^{\text{AM}}(\mathbf{x}) = -\beta^{-1} \log \left[\sum_{\mu=1}^K \exp \left(-\beta \|\mathbf{x} - \boldsymbol{\xi}^\mu\|_2^2 \right) \right] \quad (6)$$

where β is the inverse “temperature”, which controls the steepness of the energy landscape around memories $\boldsymbol{\xi}^\mu$. A direct comparison of the energy formulas (5) and (6) highlights a close connection between these two frameworks. Specifically, the data points in the diffusion model framework play the role of memories in the associative memory formulation. The variance of the noise added during the forward diffusion process (1) plays the role of the effective temperature β^{-1} . Finally, the reverse denoising process (2) corresponds to memory retrieval dynamics [36, 37].

3 Memorization-to-Generalization in 2D

To better illustrate this connection, it is instructive to investigate a simple 2-dimensional toy model, see Fig. (3), which exhibits many aspects of the memorization-generalization transition. Imagine that the training data lies on a unit circle. We are interested in exploring how the shape of the energy function (6) changes as the number of training data points increases.

[$K = 1$] For a single data point $\boldsymbol{\xi}^1$, the energy function (6) has a single local minimum at that stored pattern.

$$E^{\text{AM}}(\mathbf{x}) = -\beta^{-1} \log \left[\exp \left(-\beta \|\mathbf{x} - \boldsymbol{\xi}^1\|_2^2 \right) \right] = \|\mathbf{x} - \boldsymbol{\xi}^1\|_2^2 \quad (7)$$

The shape of the energy landscape is independent of the value of β .

[$K = 2$] For two patterns, the energy is given by

$$E^{\text{AM}}(\mathbf{x}) = -\beta^{-1} \log \left[\exp \left(-\beta \|\mathbf{x} - \boldsymbol{\xi}^1\|_2^2 \right) + \exp \left(-\beta \|\mathbf{x} - \boldsymbol{\xi}^2\|_2^2 \right) \right] \quad (8)$$

For $\beta \rightarrow \infty$, this energy has two local minima corresponding to the stored patterns. Meanwhile, for finite values of β , there exist configurations of patterns such that the energy has only one local minimum:

$$\boldsymbol{\eta} = \arg \min_{\mathbf{x}} E^{\text{AM}}(\mathbf{x}) \quad (9)$$

such that this local minimum is different from either of the two stored patterns: $\boldsymbol{\eta} \neq \boldsymbol{\xi}^1$ and $\boldsymbol{\eta} \neq \boldsymbol{\xi}^2$. This “emergent” local minimum is the *spurious state*, see also the cartoon illustration in Fig. (1).

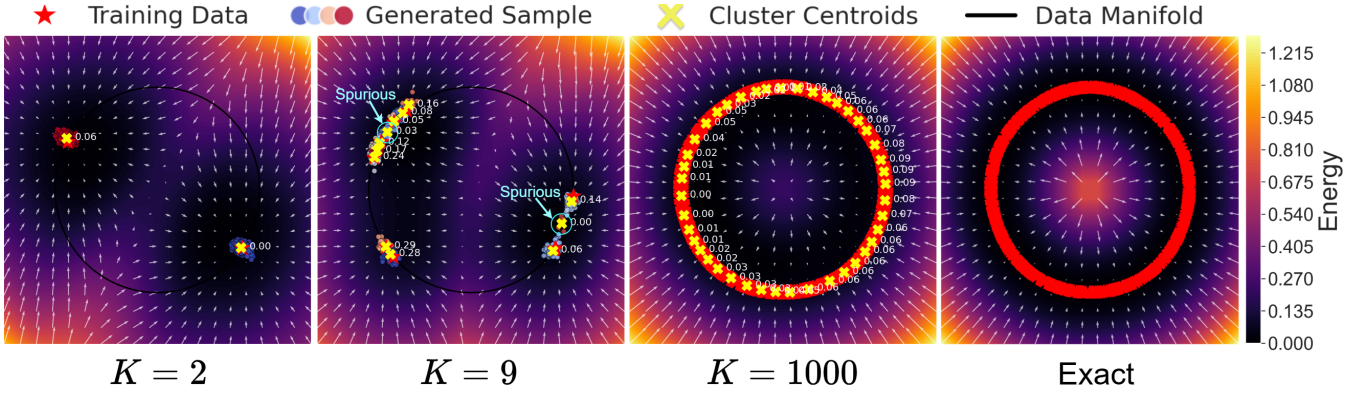


Figure 3: Energy landscape evolution for the 2D toy model as training data size K increases. Models trained at $K \in \{2, 9, 1000\}$ use standard VE-SDE based diffusion pipeline with training data sampled from the unit circle, shown in black for $K \in \{2, 9\}$. Generated samples are shown alongside the learned score field $s_\theta(\mathbf{x}_t, t)$ done via a neural network, aligned with the negative gradient of the energy (5). Hierarchical clustering identifies structure within the generations, with cluster centroid energies visualized by color and numerical value. The rightmost panel shows the exact solution as $K \rightarrow \infty$ derived in Eq. (12). As K grows, the model initially memorizes individual data points, forming isolated basins. Around $K = 9$, *spurious patterns* emerge — distinct low-energy attractors not present in the data — which mark the onset of generalization. At large K , the model enters a fully generalized regime, where low-energy states lie on a flat, continuous manifold shown in Fig. (1).

[$K \rightarrow \infty$] Finally, consider the case when the number of training data points is infinite. In this case they can be described by a continuous density of states:

$$p(\mathbf{y}) = \frac{1}{\pi} \delta(y_1^2 + y_2^2 - 1) \quad (10)$$

The probability of the generated data is proportional (up to terms independent of the state \mathbf{x}) to

$$p(\mathbf{x}) \sim \int_{-\infty}^{+\infty} dy_1 dy_2 p(\mathbf{y}) e^{-\beta \|\mathbf{x} - \mathbf{y}\|_2^2} = e^{-\beta(R^2 + 1)} I_0(2\beta R) \quad (11)$$

where $I_0(\cdot)$ is a modified Bessel function of the first kind, see Appendix (A) for more details on the derivation of Eq. (11). Thus, the energy of the model is given by

$$E^{\text{AM}}(R, \phi) = R^2 + 1 - \frac{1}{\beta} \log [I_0(2\beta R)] \underset{\beta \rightarrow \infty}{\approx} (R - 1)^2 \quad (12)$$

where R is the radius of the unit circle and ϕ is the polar angle.

Notice, the dependence on the polar angle ϕ in Eq. (12) completely disappears from the final result. The local minima of the resulting energy function form a *continuous manifold*, corresponding to $R = 1$. Data samples from the model occupy the vicinity of that manifold. This

behavior describes the fully generalized phase. In the limit of large β the energy landscape is described by a parabola centered around $R = 1$.

For a single training data point, this simple model exhibits memorization. With a few training data points, the model can either be in the memorization or spurious phase, depending on the location of those points and the value of β . For a very large number of training data points, the model is in the generalization phase. All effects perfectly align with the cartoon illustration in Fig. (1).

Overall, this calculation entirely ignores the neural network, which is used to model the score and approximate the empirical energy. There exists a logical possibility that the introduction of the neural network would entirely change the progression of distinct behaviors: memorization, spurious, generalization. To test this, we trained a set of diffusion models in this precise setting. Each model is trained on a dataset of size K . The resulting energy landscapes are shown in Fig. (3). For small number of data points, e.g., $K = 2$, the diffusion model exhibits memorization. The local minima of the energy correspond to the training data points. Importantly, at $K = 9$, we are able to observe the first signs of spurious states. At this stage, the model begins to learn emergent (different from the training data) local minima of the energy. Subsequent increase of the size of the training set leads to fully generalized behavior, which is illustrated for $K = 1000$ data points. At that stage, all of the samples from the model live in close proximity of the exact data manifold. The right panel shows the analytical expression for the energy landscape, defined by Eq. (12). Thus, the conventional diffusion modeling pipeline agrees very well with the theoretical prediction of the empirical energy. Please refer to Appendix (B) for full details on the toy model experiment.

4 Detection Metrics

The main goal of our work is to establish the existence of spurious states in diffusion models trained on natural high-dimensional datasets, not just toy model problems. With this goal in mind we design detection metrics that can classify any generated sample into one of the three categories: **memorized**, **spurious**, and **generalized** samples. Fundamentally, these metrics defined below rely on two datasets: S — the training dataset used to train the diffusion model, and S' — the synthetic dataset generated from the fully trained diffusion model. The size of the synthetic set S' is assumed to be much bigger than the training set size.

The core intuition comes from the typical energy landscape around these three distinct kinds of generated samples, see Fig. (1). **Memorized** samples are elements of the synthetic set S' , which have duplicates in the training set S . **Spurious** samples are elements of the synthetic set S' , which have duplicates in the synthetic set S' , but do not have duplicates in S . In other words, the same spurious sample appears in the synthetic set more than once. Finally, **generalized** samples are unique elements of S' , which do not have duplicates in either the synthetic set S' nor the training set S .

With this intuition in mind we examine two histograms, see Fig. (4). First, for every element of the synthetic set S' the distance to the closest nearest neighbor from the training set S is shown

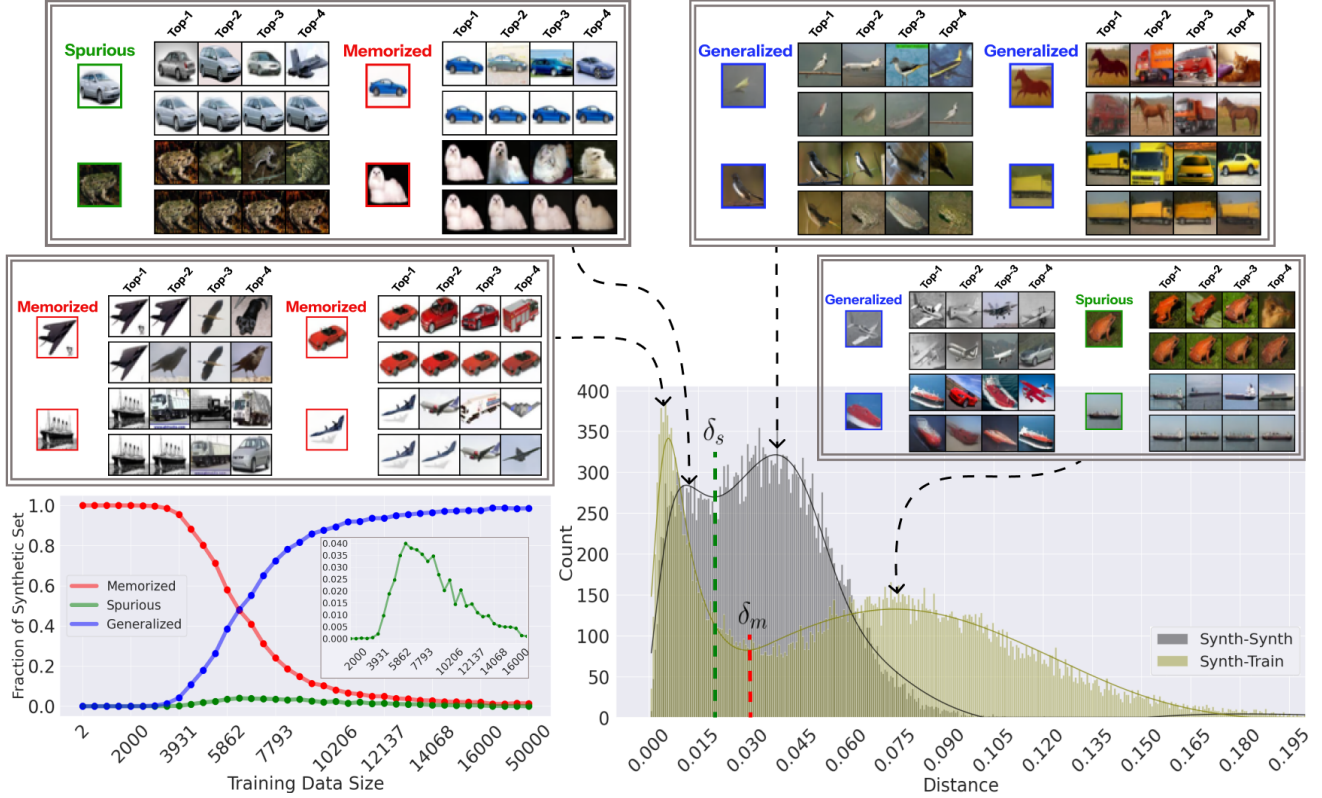


Figure 4: Different sample types across the memorization-to-generalization transition for CIFAR10 [63]. The grey histogram shows the distances between synthetic samples and their nearest neighbors from the synthetic set S' . The threshold δ_s defines a boundary between the two peaks. The olive histogram depicts the distances from the synthetic samples to their closest neighbor from the training set S , with threshold δ_m separating the two peaks. **Memorized** samples are located in the left peak of the olive histogram, below δ_m . In contrast, **generalized** and **spurious** samples appear to the right of δ_m in the olive histogram. Examples of the generated samples forming each of the four peaks of the histograms are shown in the inset frames. For each generated sample, **top-4** nearest neighbors from the training set are shown in the **top row**, and those from the synthetic set are shown in the **bottom row**. Training set size $K = 7310$ was used in this figure (peak of the frequency of spurious states), but the discussed phenomena are general and largely independent of this specific value. The fraction of the memorized, spurious, and generalized samples in the pool of all generated samples is shown in the bottom left panel as a function of the training set size. The inset shows amplified spurious fraction (green curve).

by the **olive histogram**. Second, for every element of the synthetic set S' the distance to the closest nearest neighbor in the synthetic set S' is shown by the gray histogram. Both histograms exhibit a clear bimodal shape, indicating that at least two groups of samples are present in the synthetic set. This bimodal structure makes it possible to select the memorized δ_m and spurious δ_s thresholds to separate the samples forming the two peaks in each histogram. The left peak of the **olive histogram** is composed of synthetic samples that are at a small distance away from the training set S , which can be considered as memorized samples. The left peak of the gray

histogram contains synthetic samples that have duplicates in the synthetic set S' , indicating they can be memorized if the same sample appears in the training set, or otherwise, spurious. The right peak of the gray histogram contains generalized samples, and the right peak of the olive histogram contains generalized and spurious samples. These observations make it possible to formally define the following detection metrics.

Metric 4.1 (Memorization Detection). Following [45], we define the memorization detection metric \mathcal{M} . Given a target pattern $\hat{\mathbf{x}} \in S'$ and its first nearest neighbor \mathbf{x}_1 extracted from the training set S according to a distance measure $d(\cdot, \cdot)$, where a small distance corresponds to high similarity, metric \mathcal{M} detects sample $\hat{\mathbf{x}}$ as memorized if $d(\hat{\mathbf{x}}, \mathbf{x}_1)$ is small.

$$\mathcal{M}(\hat{\mathbf{x}}, S) = \mathbb{I}\left(d(\hat{\mathbf{x}}, \mathbf{x}_1) \leq \delta_m\right) \quad (13)$$

where \mathbb{I} represents the indicator function and $\delta_m \in \mathbb{R}$ is a threshold defined by the distance histograms, see Fig. (4).

Metric 4.2 (Spurious Detection). Given a synthetic sample $\hat{\mathbf{x}}$ and its first nearest neighbor from the synthetic set $\mathbf{x}'_1 \in S'$, the spurious pattern detection metric \mathcal{S} identifies instances where the model generates outputs that do not belong to the training set but have high similarity with samples from the synthetic set (left peak of the gray histogram in Fig. (4) after the exclusion of memorized samples).

$$\mathcal{S}(\hat{\mathbf{x}}, S, S') = \mathbb{I}\left(d(\hat{\mathbf{x}}, \mathbf{x}'_1) \leq \delta_s\right) \wedge \neg \mathcal{M}(\hat{\mathbf{x}}, S) \quad (14)$$

where $\delta_s \in \mathbb{R}$ is a threshold value chosen based on the gray distance histogram, see Fig. (4).

Metric 4.3 (Generalization Detection). In contrast, the sample $\hat{\mathbf{x}}$ is generalized if it is neither memorized nor spurious.

$$\mathcal{G}(\hat{\mathbf{x}}, S, S') = \neg \mathcal{M}(\hat{\mathbf{x}}, S) \wedge \neg \mathcal{S}(\hat{\mathbf{x}}, S, S') \quad (15)$$

5 Memorization - Spurious - Generalization Transition

Using our detection metrics, we computed the fractions of memorized, spurious, and generalized samples for various sizes of training data for different datasets, see Fig. (5). These datasets include MNIST [64], FASHION-MNIST [65], CIFAR10 [63], and LSUN-CHURCH [66] scaled down to 64×64 resolution using center-crop and down-scale. For each dataset, we trained DDPM-based diffusion models [23] for $M = 38$ different training set sizes. For each model $\alpha = 1, \dots, M$, trained on the training set S_α , a synthetic set S'_α was generated. To account for duplication, we ensured that each S'_α is four times the size of its corresponding S_α , and checked that further increase of the synthetic set size does not qualitatively change our results, see Fig. (11) in Appendix (D). Each sample $\hat{\mathbf{x}} \in S'_\alpha$ is classified as either memorized, spurious, or generalized using the above metrics (13), (14), and (15). The fractions of these three pattern types with respect to the size of S'_α are plotted in Fig. (5). For each dataset, our smallest model was trained on the training

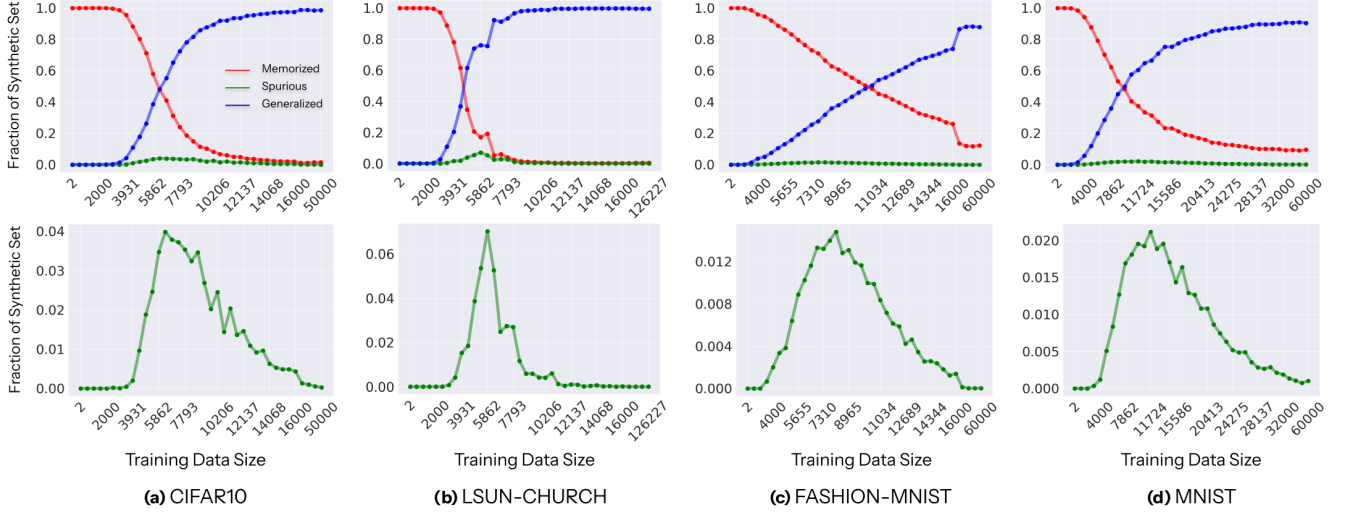


Figure 5: Fractions of **memorized**, **spurious**, and **generalized** samples in synthetic sets across training sizes and datasets. As the training data size K increases, memorization decreases and the fraction of generalized samples steadily increases (see **top row**). The fraction of spurious patterns rises and decreases at the boundary between the memorization and generalization phases (see **bottom row**).

set of $|\mathcal{S}_1| = 2$ data points while the largest model was trained on the entire original training set $\mathcal{S}_M = \mathcal{S}$. Please refer to Appendix (D) for additional details on training, selection of data sizes, and detection metrics' hyperparameters for each dataset.

The results in Fig. (5) clearly demonstrate the transition from memorization to generalization as the dataset size increases. Meanwhile, the collected samples also show distinct characteristics in each of the considered phases, see Fig. (2). Specifically, in the small data regime, we see in Fig. (5) that the diffusion model predominantly replicates the training data (see the memorized panel of Fig. (2), or additional samples in Fig. (15) of the Appendix). As the data size surpasses the memorization capacity, e.g., at $K = 3931$ for CIFAR10 in Fig. (5), we observe a critical transition where the memorization fraction declines and spurious patterns become prominent. Such patterns exhibit strong duplication in the synthetic set (see the spurious panel of Fig. (2) and additional samples in Fig. (16) of the Appendix). The emergence of such patterns aligns with the onset of generalization, as the model moves away from strictly reproducing the training set and starts generating novel combinations of learned features. Subsequent increase of the training set size leads to the decrease of the fractions of memorized and spurious samples, signaling the transition to the full generalization regime. At this stage, the model completely loses its replication ability and no duplicate samples are detected in either training or synthetic sets (see the generalized panel of Fig. (2) and additional samples in Fig. (17) of the Appendix). Overall, this particular trend is also observed as the size of the diffusion model's neural network is varied, see the results in Fig. (9) of Appendix (D).

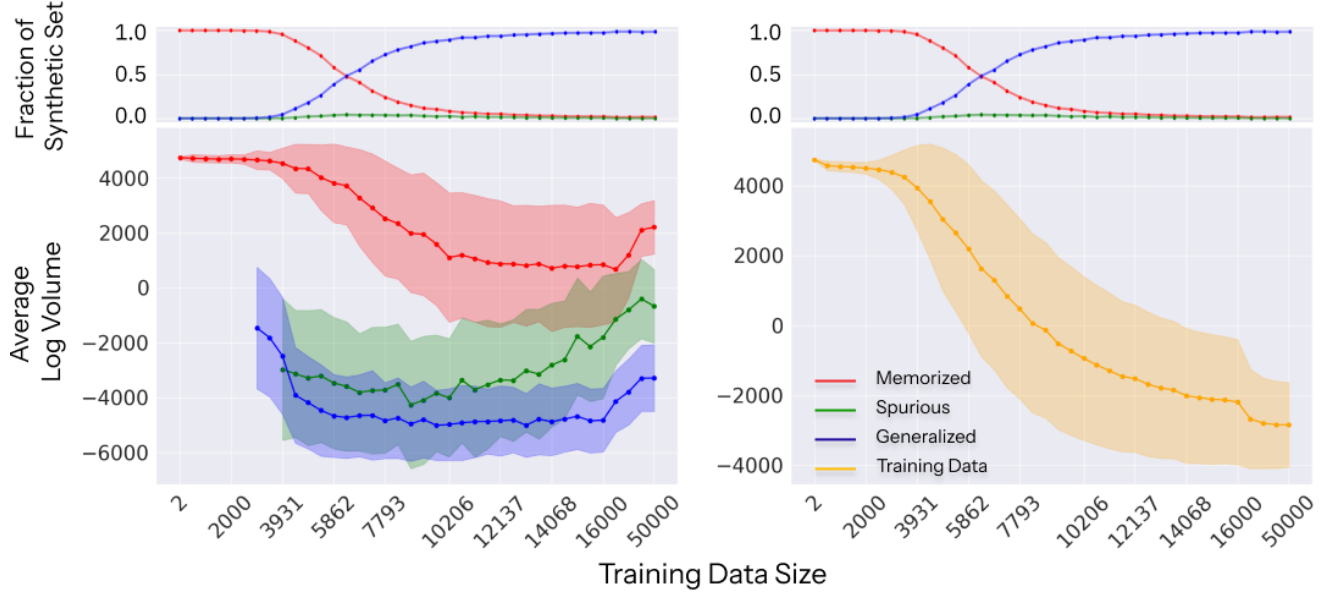


Figure 6: Average log-volume of the hyperspheric basin of attraction of different sample types as the training data size K grows, in CIFAR10 [63], computed with up to 512 samples per type. When fewer than 512 samples are available, all points are used. The log-volume of training samples and the transition plot from Fig. (5) are included to confirm the shrinking basins of attraction in diffusion models. Shaded regions indicate standard deviation of the log-volume values.

6 The Basin of Attraction Across the Transition

Diffusion models provide us with an opportunity to define the notion of basins of attraction around generated samples to further strengthen their connection to associative memories. Specifically, as the training data size K varies, the sizes of those basins for memorized, spurious, and generalized samples can exhibit interesting behaviors. This section studies these phenomena empirically.

Inspired by [38, 54, 67], we perturb a pattern \mathbf{x}_0 through the forward diffusion process for T steps, and attempt to reverse it back through the reverse diffusion process. The maximum or critical time t_c , where the reverse process can still recover the pattern \mathbf{x}_0 from its perturbation \mathbf{x}_{t_c} within an error margin $\delta \in \mathbb{R}$, defines the basin of attraction for pattern \mathbf{x}_0 . The radius of this basin $R(\mathbf{x}_0, \mathbf{x}_{t_c}) = \|\mathbf{x}_0 - \mathbf{x}_{t_c}\|$ is the Euclidean norm of the difference between \mathbf{x}_0 and its recoverable perturbation \mathbf{x}_{t_c} . This radius can be converted to volume assuming that the basin of attraction is a sphere of radius $R(\mathbf{x}_0, \mathbf{x}_{t_c})$. Please also refer to Appendix (G) for more details on the experimentation and computation of t_c and the volume.

The results for log-volume versus training size are shown in Fig. (6). The basins of attraction for training data decrease as K increases. This trend is expected, since packing larger amount of training data in a given volume of the configuration space results in a smaller volume per data point, similarly to the ideal gas in physics. Memorized samples follow a similar trend. These results suggest that as K grows, the diffusion model becomes less effective at denoising the

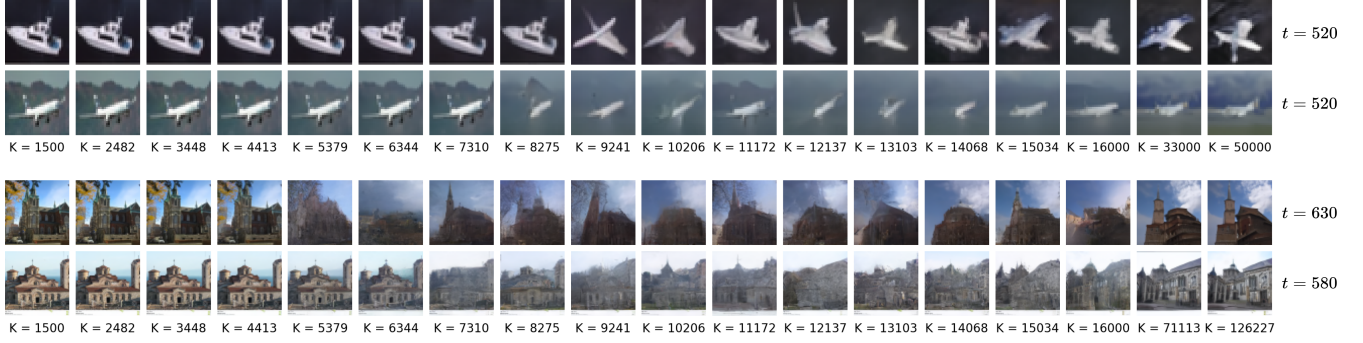


Figure 7: An illustration of the shrinkage of basins of attraction as the training data size increases. Two CIFAR10 [63] and two LSUN-CHURCH [66] training images are independently perturbed using different timesteps $t \approx t_c$ (shown on the right), each chosen near the end of the memorization phase (see Fig. (20) in the Appendix), and then denoised using the deterministic DDIM sampler [24]. At small training data sizes, the model accurately recovers the original image. As the training data size increases, denoising performance deteriorates: the model shifts from retrieval of data points to generating novel outputs. In intermediate regimes, the outputs resemble spurious patterns: partial and noise-like generations indicative of this transition.

perturbed data points, and instead gets much better at synthesizing. The most significant finding is that each of the three sample types exhibits a distinct log-volume trend: memorized samples have the largest log-volume, generalized samples have the smallest log-volume (this is expected as they should be unlikely recoverable by definition, resulting in close to zero volume), and spurious samples fall in between the two. This finding suggests a clear separation in how different sample types behave as the model’s training data size progresses. Please refer to Figs. (18) and (19) in the Appendix for the results of average log-volume across the transition for the other datasets, which exhibit the same behavior as Fig. (6).

To further illustrate the shrinkage of basins of attraction, we visualize the degradation in the denoising process as the training data size K increases, as shown in Fig. (7). For each training image, we apply the forward diffusion process using a timestep $t \approx t_c$, chosen near the end of the memorization phase (see Fig. (20) in the Appendix). The perturbed image is then denoised using the deterministic DDIM sampler [24], starting from that same timestep t , across diffusion models trained with varying K . When K is small, the diffusion model behaves like a DenseAM, effectively denoising and recovering the original image. However, as K increases, this retrieval ability weakens, and the model shifts toward generating novel samples. In the intermediate regime, before full generalization, the outputs of the denoising process visually resemble spurious patterns: incomplete or noise-like novel generations which indicate the onset of generalization. Please refer to Appendix (G) for more details on this visual demonstration.

7 The Relative Energy Gap Across the Transition

Lastly, we study how the energy of the three sample types changes as the training data size increases. Following the efficient relative energy computation from [38], we measure the relative energy gap of the three sample types with respect to that of the training data samples. Please refer to Appendix (H) for full details on the experiment and computation of the relative energy gap for different sample types.

The results are recorded in Fig. (8). For small training data sizes, the energy of the memorized samples is low and of the generalized samples is high. As K increases, the energy of the memorized samples increases, while the energy of the generalized samples decreases. The energy of the spurious states is the lowest among these three types of sample at the memorization-generalization transition. Please refer to Fig. (23) in the Appendix for the results of the average relative energy gap across the transition for the other datasets, which show a similar behavior as Fig. (8).

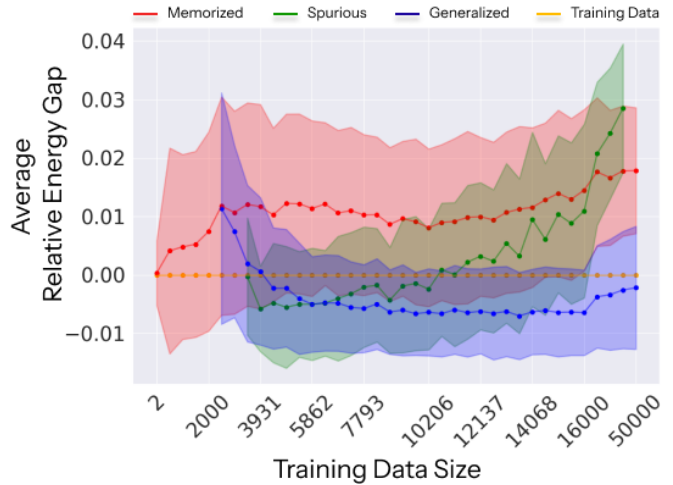


Figure 8: Average relative energy gap of each sample type and the training samples in CIFAR10 [63] as training data size K grows. The gaps are measured relative to training samples, whose energy is set to zero (energy is defined up to an additive constant). Shaded regions show standard deviation of the gap values.

8 Conclusion

In this work, we established a novel connection between diffusion models and DenseAMs. Specifically, we identified the emergence of creativity (generalization) in diffusion models with the failure of successful memory recalls, via an energy-based theoretical description of diffusion models. Using this theory, we identified a novel phase – *spurious states* – previously overlooked in the memorization-generalization literature. Finally, we established that diffusion models trained on natural datasets follow the same transition (memorization to spurious phase to generalization) as predicted by our theory. The peak frequency of spurious states among generated samples marks the onset of generalization as the training set size increases. The volume measurements and relative energy gap analysis of different sample types, across multiple datasets consistently support this three distinct phases of computation, providing a comprehensive understanding of how diffusion models evolve from memorization to generalization as the amount of training data increases.

Acknowledgments

M.N. acknowledges the support of PNRR MUR project PE0000013-FAIR.

B.P. acknowledges the support of IBM through the IBM-Rensselaer Future of Computing Research Collaboration (FCRC).

References

- [1] John J. Hopfield. Neural networks and physical systems with emergent collective computational abilities. *Proceedings of the National Academy of Sciences*, 79(8):2554–2558, 1982.
- [2] John J Hopfield. Neurons with graded response have collective computational properties like those of two-state neurons. *Proceedings of the national academy of sciences*, 81(10):3088–3092, 1984.
- [3] S-I Amari. Learning patterns and pattern sequences by self-organizing nets of threshold elements. *IEEE Transactions on computers*, 100(11):1197–1206, 1972.
- [4] Dmitry Krotov and John J. Hopfield. Dense associative memory for pattern recognition. In D. Lee, M. Sugiyama, U. Luxburg, I. Guyon, and R. Garnett, editors, *Advances in Neural Information Processing Systems*, volume 29. Curran Associates, Inc., 2016.
- [5] Dmitry Krotov and John Hopfield. Dense associative memory is robust to adversarial inputs. *Neural computation*, 30(12):3151–3167, 2018.
- [6] Mete Demircigil, Judith Heusel, Matthias Löwe, Sven Upgang, and Franck Vermet. On a model of associative memory with huge storage capacity. *Journal of Statistical Physics*, 168(2):288–299, May 2017.
- [7] Elena Agliari, Francesco Alemanno, Adriano Barra, Martino Centonze, and Alberto Fachechi. Neural networks with a redundant representation: Detecting the undetectable. *Physical review letters*, 124(2):028301, 2020.
- [8] Elena Agliari and Giordano De Marzo. Tolerance versus synaptic noise in dense associative memories. *The European Physical Journal Plus*, 135(11):1–22, 2020.
- [9] Dmitry Krotov. Hierarchical associative memory. *arXiv preprint 2107.06446*, 2021.
- [10] Linda Albanese, Francesco Alemanno, Andrea Alessandrelli, and Adriano Barra. Replica symmetry breaking in dense hebbian neural networks. *Journal of Statistical Physics*, 189(2):24, 2022.
- [11] Beren Millidge, Tommaso Salvatori, Yuhang Song, Thomas Lukasiewicz, and Rafal Bogacz. Universal hopfield networks: A general framework for single-shot associative memory models. In *International Conference on Machine Learning*, pages 15561–15583. PMLR, 2022.
- [12] Bishwajit Saha, Dmitry Krotov, Mohammed J Zaki, and Parikshit Ram. End-to-end differentiable clustering with associative memories. In *International Conference on Machine Learning*, pages 29649–29670. PMLR, 2023.
- [13] Benjamin Hoover, Yuchen Liang, Bao Pham, Rameswar Panda, Hendrik Strobelt, Duen Horng Chau, Mohammed Zaki, and Dmitry Krotov. Energy transformer. In A. Oh, T. Neumann, A. Globerson, K. Saenko, M. Hardt, and S. Levine, editors, *Advances in Neural Information Processing Systems*, volume 36, pages 27532–27559. Curran Associates, Inc., 2023.

- [14] Hamza Chaudhry, Jacob Zavatone-Veth, Dmitry Krotov, and Cengiz Pehlevan. Long sequence hopfield memory. *Advances in Neural Information Processing Systems*, 36:54300–54340, 2023.
- [15] Ryo Karakida, Toshihiro Ota, and Masato Taki. Hierarchical associative memory, parallelized mlp-mixer, and symmetry breaking. *arXiv preprint arXiv:2406.12220*, 2024.
- [16] Saul José Rodrigues dos Santos, Vlad Niculae, Daniel C McNamee, and Andre Martins. Sparse and structured hopfield networks. In *Forty-first International Conference on Machine Learning*, 2024.
- [17] Linda Albanese, Andrea Alessandrelli, Alessia Annibale, and Adriano Barra. About the de almeida–thouless line in neural networks. *Physica A: Statistical Mechanics and its Applications*, 633:129372, 2024.
- [18] Benjamin Hoover, Duen Horng Chau, Hendrik Strobelt, Parikshit Ram, and Dmitry Krotov. Dense associative memory through the lens of random features. In *The Thirty-eighth Annual Conference on Neural Information Processing Systems*, 2024.
- [19] Hubert Ramsauer, Bernhard Schäfl, Johannes Lehner, Philipp Seidl, Michael Widrich, Lukas Gruber, Markus Holzleitner, Thomas Adler, David Kreil, Michael K Kopp, Günter Klambauer, Johannes Brandstetter, and Sepp Hochreiter. Hopfield networks is all you need. In *International Conference on Learning Representations*, 2021.
- [20] Dmitry Krotov and John J Hopfield. Large associative memory problem in neurobiology and machine learning. In *International Conference on Learning Representations*, 2021.
- [21] Leo Kozachkov, Jean-Jacques Slotine, and Dmitry Krotov. Neuron–astrocyte associative memory. *Proceedings of the National Academy of Sciences*, 122(21):e2417788122, 2025.
- [22] Jascha Sohl-Dickstein, Eric Weiss, Niru Maheswaranathan, and Surya Ganguli. Deep unsupervised learning using nonequilibrium thermodynamics. In *International Conference on Machine Learning*, 2015.
- [23] Jonathan Ho, Ajay Jain, and Pieter Abbeel. Denoising diffusion probabilistic models. *Advances in Neural Information Processing Systems*, 2020.
- [24] Jiaming Song, Chenlin Meng, and Stefano Ermon. Denoising diffusion implicit models. *arXiv preprint arXiv:2010.02502*, 2020.
- [25] Yang Song, Jascha Sohl-Dickstein, Diederik P Kingma, Abhishek Kumar, Stefano Ermon, and Ben Poole. Score-based generative modeling through stochastic differential equations. In *International Conference on Learning Representations*, 2021.
- [26] Nanxin Chen, Yu Zhang, Heiga Zen, Ron J Weiss, Mohammad Norouzi, and William Chan. Wavegrad: Estimating gradients for waveform generation. *arXiv preprint arXiv:2009.00713*, 2020.
- [27] Zhifeng Kong, Wei Ping, Jiaji Huang, Kexin Zhao, and Bryan Catanzaro. Diffwave: A versatile diffusion model for audio synthesis. *arXiv preprint arXiv:2009.09761*, 2020.

[28] Haohe Liu, Zehua Chen, Yi Yuan, Xinhao Mei, Xubo Liu, Danilo Mandic, Wenwu Wang, and Mark D Plumbley. AudioLDM: Text-to-audio generation with latent diffusion models. In *Proceedings of the 40th International Conference on Machine Learning*, volume 202, pages 21450–21474, 2023.

[29] Jonathan Ho, Tim Salimans, Alexey Gritsenko, William Chan, Mohammad Norouzi, and David J Fleet. Video diffusion models. *arXiv preprint arXiv:2204.03458*, 2022.

[30] Uriel Singer, Adam Polyak, Thomas Hayes, Xi Yin, Jie An, Songyang Zhang, Qiyuan Hu, Harry Yang, Oron Ashual, Oran Gafni, et al. Make-a-video: Text-to-video generation without text-video data. *arXiv preprint arXiv:2209.14792*, 2022.

[31] Andreas Blattmann, Robin Rombach, Huan Ling, Tim Dockhorn, Seung Wook Kim, Sanja Fidler, and Karsten Kreis. Align your latents: High-resolution video synthesis with latent diffusion models. In *IEEE Conference on Computer Vision and Pattern Recognition (CVPR)*, 2023.

[32] Tim Brooks, Bill Peebles, Connor Holmes, Will DePue, Yufei Guo, Li Jing, David Schnurr, Joe Taylor, Troy Luhman, Eric Luhman, Clarence Ng, Ricky Wang, and Aditya Ramesh. Video generation models as world simulators, 2024.

[33] Gowthami Somepalli, Vasu Singla, Micah Goldblum, Jonas Geiping, and Tom Goldstein. Diffusion art or digital forgery? investigating data replication in diffusion models. In *Proceedings of the IEEE/CVF Conference on Computer Vision and Pattern Recognition*, pages 6048–6058, 2023.

[34] Gowthami Somepalli, Vasu Singla, Micah Goldblum, Jonas Geiping, and Tom Goldstein. Understanding and mitigating copying in diffusion models. *Advances in Neural Information Processing Systems*, 36:47783–47803, 2023.

[35] Nicolas Carlini, Jamie Hayes, Milad Nasr, Matthew Jagielski, Vikash Sehwag, Florian Tramer, Borja Balle, Daphne Ippolito, and Eric Wallace. Extracting training data from diffusion models. In *32nd USENIX Security Symposium (USENIX Security 23)*, pages 5253–5270, 2023.

[36] Benjamin Hoover, Hendrik Strobelt, Dmitry Krotov, Judy Hoffman, Zsolt Kira, and Duen Horng Chau. Memory in plain sight: A survey of the uncanny resemblances between diffusion models and associative memories. *arXiv preprint arXiv:2309.16750*, 2023.

[37] Luca Ambrogioni. In search of dispersed memories: Generative diffusion models are associative memory networks. *Entropy*, 26(5):381, 2024.

[38] Gabriel Raya and Luca Ambrogioni. Spontaneous symmetry breaking in generative diffusion models. *Advances in Neural Information Processing Systems*, 36, 2024.

[39] John J. Hopfield, David I. Feinstein, and Richard G. Palmer. ‘unlearning’ has a stabilizing effect in collective memories. *Nature*, 304:158–159, 1983.

[40] Daniel J. Amit, Hanoch Gutfreund, and H. Sompolinsky. Storing infinite numbers of patterns

in a spin-glass model of neural networks. *Phys. Rev. Lett.*, 55:1530–1533, Sep 1985.

- [41] Y. Abu-Mostafa and J. St. Jacques. Information capacity of the hopfield model. *IEEE Transactions on Information Theory*, 31(4):461–464, 1985.
- [42] Silvio Kalaj, Clarissa Lauditi, Gabriele Perugini, Carlo Lucibello, Enrico M Malatesta, and Matteo Negri. Random features hopfield networks generalize retrieval to previously unseen examples. *arXiv preprint arXiv:2407.05658*, 2024.
- [43] Casey Meehan, Kamalika Chaudhuri, and Sanjoy Dasgupta. A non-parametric test to detect data-copying in generative models. In *International Conference on Artificial Intelligence and Statistics*, 2020.
- [44] Gerrit J.J. Van den Burg and Chris Williams. On memorization in probabilistic deep generative models. In A. Beygelzimer, Y. Dauphin, P. Liang, and J. Wortman Vaughan, editors, *Advances in Neural Information Processing Systems*, 2021.
- [45] TaeHo Yoon, Joo Young Choi, Sehyun Kwon, and Ernest K Ryu. Diffusion probabilistic models generalize when they fail to memorize. In *ICML 2023 Workshop on Structured Probabilistic Inference Generative Modeling*, 2023.
- [46] Xiangming Gu, Chao Du, Tianyu Pang, Chongxuan Li, Min Lin, and Ye Wang. On memorization in diffusion models. *arXiv preprint arXiv:2310.02664*, 2023.
- [47] Puheng Li, Zhong Li, Huishuai Zhang, and Jiang Bian. On the generalization properties of diffusion models. *Advances in Neural Information Processing Systems*, 36, 2024.
- [48] Zahra Kadkhodaie, Florentin Guth, Eero P Simoncelli, and Stéphane Mallat. Generalization in diffusion models arises from geometry-adaptive harmonic representation. *arXiv preprint arXiv:2310.02557*, 2023.
- [49] Enrico Ventura, Beatrice Achilli, Gianluigi Silvestri, Carlo Lucibello, and Luca Ambrogioni. Manifolds, random matrices and spectral gaps: The geometric phases of generative diffusion. *arXiv preprint arXiv:2410.05898*, 2024.
- [50] Beatrice Achilli, Enrico Ventura, Gianluigi Silvestri, Bao Pham, Gabriel Raya, Dmitry Krotov, Carlo Lucibello, and Luca Ambrogioni. Losing dimensions: Geometric memorization in generative diffusion. *arXiv preprint arXiv:2410.08727*, 2024.
- [51] Mason Kamb and Surya Ganguli. An analytic theory of creativity in convolutional diffusion models. *arXiv preprint arXiv:2412.20292*, 2024.
- [52] Brendan Leigh Ross, Hamidreza Kamkari, Tongzi Wu, Rasa Hosseinzadeh, Zhaoyan Liu, George Stein, Jesse C Cresswell, and Gabriel Loaiza-Ganem. A geometric framework for understanding memorization in generative models. *arXiv preprint arXiv:2411.00113*, 2024.
- [53] Hugo Cui, Cengiz Pehlevan, and Yue M Lu. A precise asymptotic analysis of learning diffusion models: theory and insights. *arXiv preprint arXiv:2501.03937*, 2025.
- [54] Giulio Biroli, Tony Bonnaire, Valentin de Bortoli, and Marc Mézard. Dynamical regimes of

diffusion models. *Nature Communications*, 15(1), November 2024.

- [55] Beatrice Achilli, Luca Ambrogioni, Carlo Lucibello, Marc Mézard, and Enrico Ventura. Memorization and generalization in generative diffusion under the manifold hypothesis. *arXiv preprint arXiv:2502.09578*, 2025.
- [56] Aapo Hyvärinen. Estimation of non-normalized statistical models by score matching. *Journal of Machine Learning Research*, 6(24):695–709, 2005.
- [57] Pascal Vincent. A connection between score matching and denoising autoencoders. *Neural Computation*, 23(7):1661–1674, 2011.
- [58] Yang Song and Stefano Ermon. Generative modeling by estimating gradients of the data distribution. *Advances in neural information processing systems*, 32, 2019.
- [59] Anand Jerry George, Rodrigo Veiga, and Nicolas Macris. Analysis of diffusion models for manifold data. *arXiv preprint arXiv:2502.04339*, 2025.
- [60] Giulio Biroli and Marc Mézard. Generative diffusion in very large dimensions. *Journal of Statistical Mechanics: Theory and Experiment*, 2023(9):093402, 2023.
- [61] John J Vastola. Generalization through variance: how noise shapes inductive biases in diffusion models. *arXiv preprint arXiv:2504.12532*, 2025.
- [62] Dmitry Krotov. A new frontier for hopfield networks. *Nature Reviews Physics*, 5(7):366–367, 2023.
- [63] Alex Krizhevsky, Vinod Nair, and Geoffrey Hinton. The cifar-10 dataset. *online: http://www.cs.toronto.edu/kriz/cifar.html*, 55(5):2, 2014.
- [64] Li Deng. The mnist database of handwritten digit images for machine learning research [best of the web]. *IEEE Signal Processing Magazine*, 29(6):141–142, 2012.
- [65] Han Xiao, Kashif Rasul, and Roland Vollgraf. Fashion-mnist: a novel image dataset for benchmarking machine learning algorithms. *arXiv preprint 1708.07747*, 2017.
- [66] Fisher Yu, Yinda Zhang, Shuran Song, Ari Seff, and Jianxiong Xiao. Lsun: Construction of a large-scale image dataset using deep learning with humans in the loop. *arXiv preprint arXiv:1506.03365*, 2015.
- [67] Marvin Li and Sitan Chen. Critical windows: non-asymptotic theory for feature emergence in diffusion models. *arXiv preprint arXiv:2403.01633*, 2024.
- [68] Izrail Solomonovich Gradshteyn and Iosif Moiseevich Ryzhik. *Table of integrals, series, and products*. Academic press, 2014.
- [69] Prajit Ramachandran, Barret Zoph, and Quoc V. Le. Searching for activation functions. *CoRR*, abs/1710.05941, 2017.
- [70] Diederik P. Kingma and Jimmy Ba. Adam: A method for stochastic optimization, 2017.

[71] Peter E Kloeden, Eckhard Platen, Peter E Kloeden, and Eckhard Platen. *Stochastic differential equations*. Springer, 1992.

[72] Ricky T. Q. Chen, Yulia Rubanova, Jesse Bettencourt, and David Duvenaud. Neural ordinary differential equations. In *Proceedings of the 32nd International Conference on Neural Information Processing Systems*, NIPS’18, page 6572–6583, Red Hook, NY, USA, 2018. Curran Associates Inc.

[73] Michael F Hutchinson. A stochastic estimator of the trace of the influence matrix for laplacian smoothing splines. *Communications in Statistics-Simulation and Computation*, 18(3):1059–1076, 1989.

[74] J.R. Dormand and P.J. Prince. A family of embedded runge-kutta formulae. *Journal of Computational and Applied Mathematics*, 6(1):19–26, 1980.

[75] Pauli Virtanen, Ralf Gommers, Travis E. Oliphant, Matt Haberland, Tyler Reddy, David Cournapeau, Evgeni Burovski, Pearu Peterson, Warren Weckesser, Jonathan Bright, Stéfan J. van der Walt, Matthew Brett, Joshua Wilson, K. Jarrod Millman, Nikolay Mayorov, Andrew R. J. Nelson, Eric Jones, Robert Kern, Eric Larson, C J Carey, İlhan Polat, Yu Feng, Eric W. Moore, Jake VanderPlas, Denis Laxalde, Josef Perktold, Robert Cimrman, Ian Henriksen, E. A. Quintero, Charles R. Harris, Anne M. Archibald, Antônio H. Ribeiro, Fabian Pedregosa, Paul van Mulbregt, and SciPy 1.0 Contributors. SciPy 1.0: Fundamental Algorithms for Scientific Computing in Python. *Nature Methods*, 17:261–272, 2020.

[76] Bernt Oksendal. *Stochastic differential equations (3rd ed.): an introduction with applications*. Springer-Verlag, Berlin, Heidelberg, 1992.

[77] Richard Zhang, Phillip Isola, Alexei A Efros, Eli Shechtman, and Oliver Wang. The unreasonable effectiveness of deep features as a perceptual metric. In *CVPR*, 2018.

[78] Alex Krizhevsky, Ilya Sutskever, and Geoffrey E Hinton. Imagenet classification with deep convolutional neural networks. In F. Pereira, C.J. Burges, L. Bottou, and K.Q. Weinberger, editors, *Advances in Neural Information Processing Systems*, volume 25. Curran Associates, Inc., 2012.

[79] Aaron Van den Oord, Nal Kalchbrenner, Lasse Espeholt, Oriol Vinyals, and Alex Graves. Conditional image generation with pixelcnn decoders. *Advances in neural information processing systems*, 29, 2016.

[80] Tim Salimans, Andrej Karpathy, Xi Chen, and Diederik P Kingma. Pixelcnn++: Improving the pixelcnn with discretized logistic mixture likelihood and other modifications. *arXiv preprint arXiv:1701.05517*, 2017.

[81] Kaiming He, Xiangyu Zhang, Shaoqing Ren, and Jian Sun. Deep residual learning for image recognition. In *Proceedings of the IEEE conference on computer vision and pattern recognition*, pages 770–778, 2016.

[82] Karen Simonyan and Andrew Zisserman. Very deep convolutional networks for large-scale

image recognition. *arXiv preprint arXiv:1409.1556*, 2014.

[83] Pascal Sebah and Xavier Gourdon. Introduction to the gamma function. *American Journal of Scientific Research*, 2, 2002.

A Additional Details on the Energy Formulation of the 2D Toy Example

In order to obtain Eq. (11), it is easiest to introduce polar coordinates for both the state vector \mathbf{x} and the training data \mathbf{y} :

$$\begin{cases} x_1 = R \cos(\phi) \\ x_2 = R \sin(\phi) \end{cases} \quad \begin{cases} y_1 = r \cos(\varphi) \\ y_2 = r \sin(\varphi) \end{cases}$$

The integral (11) can then be written as

$$p(\mathbf{x}) \sim \int_0^{2\pi} d\varphi \int_0^\infty r dr \frac{1}{\pi} \delta(r^2 - 1) e^{-\beta[R^2 + r^2 - 2Rr \cos(\varphi - \phi)]} = e^{-\beta(R^2 + 1)} I_0(2\beta R)$$

and explicitly computed using the definition of the modified Bessel functions [68].

B Experimental Details of the 2D Toy Example

This section describes the two-dimensional toy example used in Section (3), including details about the neural network architecture, training, generation, and computation of the model’s energy. All of the corresponding code will be made publicly available.

Dataset. To construct the dataset, we uniformly sample points on the unit circle. Concretely, we take $\mathbf{y} \sim p(\mathbf{y}) = \frac{1}{2\pi} \delta(r - 1)$, where $r = \sqrt{y_1^2 + y_2^2}$ is the radius and $\delta(r - 1)$ is the delta function ensures that all probability mass lies on radius $r = 1$. The factor $\frac{1}{2\pi}$ guarantees that the angles are sampled uniformly, relying on the identity $\delta(\sqrt{y_1^2 + y_2^2} - 1) = 2\delta(y_1^2 + y_2^2 - 1)$ in $p(\mathbf{y}) = \frac{1}{\pi} \delta(y_1^2 + y_2^2 - 1)$. In practice, we sample polar coordinates (r, φ) with $r = 1$ and uniformly sample the angular coordinate φ from $[0, 2\pi]$. We then convert (r, φ) to Cartesian coordinates (y_1, y_2) using $y_1 = r \cos \varphi$ and $y_2 = r \sin \varphi$.

We first created a data set of 60000 points using a fixed random seed, then built smaller subsets (e.g., $K \in \{2, 4, 9, 1000, 10000\}$) by progressively adding distinct samples without replacement, ensuring that each subset is a strict subset of the next. This approach allows us to systematically examine how the model behaves, as we vary the size of the training set.

Exact Score. Following Eq. (12) specified in Section (3), energy can be written in closed form, whose local minima form the continuous data manifold at $R = 1$ (throughout this paper we use r for the polar radius of the training data and R for the polar radius of the generated samples). Furthermore, in the case of many data points or $K \rightarrow \infty$, we have $p(\mathbf{y}) = \frac{1}{\pi} \delta(y_1^2 + y_2^2 - 1)$. Since

$p(R) \propto \exp^{-E^{\text{AM}}(R)}$, the score can be described as

$$\begin{aligned} -\nabla_R \log p(R) &= \nabla_R E^{\text{AM}}(R) \\ &= 2R - \frac{2\beta I_1(2\beta R)}{\beta I_0(2\beta R)} \\ &= 2R - 2 \frac{I_1(2\beta R)}{I_0(2\beta R)} \end{aligned} \quad (16)$$

where $E^{\text{AM}}(R)$ is Eq. (12), and I_1 and I_0 are the first-order and zero-order modified Bessel functions of the first kind, respectively. With further expansion, the score becomes

$$\nabla_R \log p(R) = 2 \left(\frac{I_1(2\beta R)}{I_0(2\beta R)} - R \right) \quad \Rightarrow \quad \nabla_x \log p(x) = 2 \left(\frac{I_1(2\beta R)}{I_0(2\beta R)} - R \right) \frac{x}{R} \quad (17)$$

We implemented Eq. (12) on a 20×20 grid to obtain the exact energy and score of the model, overlaying 1000 samples from the training set. For visualization purposes, we set $\beta = 20$, ensuring a well-defined energy landscape. Additionally, we normalized the energy by subtracting its minimum value to ensure that the lowest energy point remains at zero.

VE-SDE. To align with the theoretical framework, we employ a variance exploding (VE) SDE of the form

$$d\mathbf{x}_t = \sigma d\mathbf{w}_t \quad (18)$$

where the diffusion coefficient $g(t) = \sigma$. Assuming $t \in (0, 1]$, the variance of the diffusion kernel is given by $\int_0^t g^2(s) ds = \sigma^2 t$, which allows us to construct the corresponding Gaussian kernel

$$p(\mathbf{x}_t | \mathbf{y}) = \mathcal{N}(\mathbf{x}_t; \mathbf{y}, \sigma^2 t \mathbf{I})$$

However, in practice we used $t \in [\epsilon, 1]$ with $\epsilon = 10^{-5}$ for numerical stability. The generative dynamics are given by

$$d\mathbf{x}_t = [-\sigma^2 \nabla_{\mathbf{x}_t} \log p_t(\mathbf{x}_t)] dt + \sigma^2 d\mathbf{w}_t. \quad (19)$$

where this runs backwards in time to match the description of [25]. The deterministic Probability Flow ODE is

$$\frac{d\mathbf{x}_t}{dt} = -\frac{1}{2} \sigma^2 \nabla_{\mathbf{x}_t} \log p_t(\mathbf{x}_t) \quad (20)$$

which shares the same marginal distributions as the SDE in Eq. (19) and is useful for likelihood estimation.

Model and Training Details. For each training size K in Fig. (3), we use a U-Net inspired MLP-based network to estimate the score $s_\theta(\mathbf{x}_t, t)$, without using any down- or up-sampling blocks. The general architecture includes (1) a Fourier random feature (FRF) timestep embedding layer and a linear layer which projects the concatenation of FRF timestep embedding and input into a latent dimension of 256; (2) an encoder which consists of four non-convolutional residual blocks (using the same latent dimension) with Swish [69] activation in between; (3) a decoder which consists of the same number of residual blocks; and (4) a linear block which projects the latent variable back to the 2D space.

The network was trained in continuous time (with 1000 discretized steps) with $\sigma = 1$ using the objective function from [23, 25]. Optimization is performed using the Adam [70] optimizer with a learning rate $lr = 10^{-4}$. The batch size is set to $\min(K, 500)$. All models are trained for 800000 iterations with the maximum batch size of 500. Meanwhile, we use Euler-Maruyama discretization method [71] to solve Eq. (19) of the reverse SDE for the generation of samples.

Empirical distribution. We represent the data as an empirical distribution

$$p(\mathbf{y}) = \frac{1}{K} \sum_{\mu=1}^K \delta^{(N)}(\mathbf{y} - \boldsymbol{\xi}^\mu) \quad (21)$$

where N is the dimensionality of the data point \mathbf{y} . Since \mathbf{x}_t is drawn from the forward process distribution $p(\mathbf{x}_t | \mathbf{y})$ that is conditioned on the data point \mathbf{y} , which can be expressed as a Gaussian kernel $\mathcal{N}(\mathbf{x}_t; \mathbf{y}, \sigma^2 t \mathbf{I})$. We can obtain the distribution $p(\mathbf{x}_t, t)$ as

$$\begin{aligned} p(\mathbf{x}_t, t) &= \int p(\mathbf{x}_t | \mathbf{y}) p(\mathbf{y}) d\mathbf{y} = \frac{1}{K} \sum_{\mu=1}^K \int \mathcal{N}(\mathbf{x}_t; \mathbf{y}, \sigma^2 t \mathbf{I}) \delta^{(N)}(\mathbf{y} - \boldsymbol{\xi}^\mu) d\mathbf{y} \\ &= \frac{1}{K} \sum_{\mu=1}^K \mathcal{N}(\mathbf{x}_t; \boldsymbol{\xi}^\mu, \sigma^2 t \mathbf{I}) \\ &= \frac{1}{K} \sum_{\mu=1}^K \frac{1}{(2\pi \sigma^2 t)^{\frac{N}{2}}} \exp\left(-\frac{\|\mathbf{x}_t - \boldsymbol{\xi}^\mu\|_2^2}{2\sigma^2 t}\right) \end{aligned} \quad (22)$$

which is Eq. (4), when the variance of the Gaussian kernel is $\sigma^2 t$.

Likelihood Computation. Following [25] we can compute the log-likelihood $\log p_\theta(\mathbf{x}_0)$ given by a diffusion model, with the instantaneous change of variable formula [72], where \mathbf{x}_0 are the generated samples from the model. Replacing Eq. (19) into the log-likelihood equation,

$$\log p_0(\mathbf{x}_0; \theta) = \log p_T(\mathbf{x}_T) + \int_0^T \nabla \cdot \tilde{\mathbf{f}}(\mathbf{x}_t, t) dt, \quad \text{with } \tilde{\mathbf{f}}(\mathbf{x}_t, t) = -\frac{1}{2} \sigma^2 \nabla_{\mathbf{x}_t} \log p_t(\mathbf{x}_t) \quad (23)$$

The function $\tilde{\mathbf{f}}(\mathbf{x}_t, t)$ came from the above Probability Flow ODE (Eq. (20)), and $\nabla \cdot \tilde{\mathbf{f}}(\mathbf{x}_t, t)$ denotes the divergence of the function (or the trace of its Jacobian).

To estimate the likelihood of the model, we integrate $\nabla \cdot \tilde{\mathbf{f}}(\mathbf{x}_t, t)$ from a small time $\epsilon = 10^{-5}$ to $T = 1$ using a numerical integrator and add the prior logarithmic likelihood to it following Eq. (23). The divergence term $\nabla \cdot \tilde{\mathbf{f}}(\mathbf{x}_t, t)$ is computed using the Laplacian, which is computationally feasible for this toy example, instead of using the Hutchinson trace estimator [73] done in [25]. We use the RK45 method [74] implemented in the ODE solver `scipy.integrate.solve_ivp` from Scipy [75] to solve the above integral.

Energy Computation. To compute the energy, we use Eq. (5), which can be also computed using Eq. (23). From the Boltzmann distribution $p(\mathbf{x}) = \frac{1}{Z} \exp[-\beta E(\mathbf{x})]$, we obtained $\log p(\mathbf{x}) \propto$

$-\beta E(\mathbf{x})$. In our case the inverse temperature is $\beta = \frac{1}{2\sigma^2 t}$. The equation for our VE-SDE thus becomes

$$E^{\text{DM}}(\mathbf{x}_t, t) = -2\sigma^2 t \log p(\mathbf{x}_t, t) \quad (24)$$

To visualize the energy landscape, we observe the energy at $t = 0.15$ which corresponds to $\beta = 3.3$.

Sample Clustering. To cluster the generated samples, we use the `AgglomerativeClustering` algorithm from scikit-learn, which is a part of SciPy [75].

C Additional Details on the Likelihood of Diffusion Models

For concreteness, we further explain the likelihood computation in Eq. (23) within this section. Specifically, we want to highlight the formulation done by [25, 72] which resulted in Eq. (23).

Probability Flow ODE. Suppose we have the following forward process

$$d\mathbf{x}_t = \mathbf{f}(\mathbf{x}_t, t)dt + \mathbf{g}(\mathbf{x}_t, t)d\mathbf{w}_t \quad (25)$$

where $\mathbf{f}(\cdot, t) : \mathbb{R}^N \rightarrow \mathbb{R}^N$, $\mathbf{g}(\cdot, t) : \mathbb{R}^N \rightarrow \mathbb{R}^{N \times N}$ and N denotes the dimensionality of \mathbf{x}_t . Using the derivations done by [25] in their Appendix D, the evolution of the marginal probability density $p_t(\mathbf{x}_t)$ is

$$\frac{\partial p_t(\mathbf{x}_t)}{\partial t} = - \sum_{i=1}^N \frac{\partial}{\partial x_i} [f_i(\mathbf{x}_t, t)p_t(\mathbf{x}_t)] + \frac{1}{2} \sum_{i=1}^N \sum_{j=1}^N \frac{\partial^2}{\partial x_i \partial x_j} \left[\sum_{k=1}^N g_{ij}(\mathbf{x}_t, t)g_{jk}(\mathbf{x}_t, t)p_t(\mathbf{x}_t) \right] \quad (26)$$

which corresponds to Fokker-Planck equation [76]:

$$\begin{aligned} \frac{\partial p_t(\mathbf{x}_t)}{\partial t} &= - \sum_{i=1}^N \frac{\partial}{\partial x_i} [f_i(\mathbf{x}_t, t)p_t(\mathbf{x}_t)] + \frac{1}{2} \sum_{i=1}^N \frac{\partial}{\partial x_i} \left[\sum_{j=1}^N \frac{\partial}{\partial x_j} \left[\sum_{k=1}^N g_{ij}(\mathbf{x}_t, t)g_{jk}(\mathbf{x}_t, t)p_t(\mathbf{x}_t) \right] \right] \\ &= - \sum_{i=1}^N \frac{\partial}{\partial x_i} [f_i(\mathbf{x}_t, t)p_t(\mathbf{x}_t)] \\ &\quad + \frac{1}{2} \sum_{i=1}^N \frac{\partial}{\partial x_i} \left[p_t(\mathbf{x}_t) \nabla \cdot [\mathbf{g}(\mathbf{x}_t, t)\mathbf{g}(\mathbf{x}_t, t)^\top] + p_t(\mathbf{x}_t) [\mathbf{g}(\mathbf{x}_t, t)\mathbf{g}(\mathbf{x}_t, t)^\top] \nabla_{\mathbf{x}_t} \log p_t(\mathbf{x}_t) \right] \\ &= - \sum_{i=1}^N \frac{\partial}{\partial x_i} \left\{ f_i(\mathbf{x}_t, t)p_t(\mathbf{x}_t) \right. \\ &\quad \left. - \frac{1}{2} \left[\nabla \cdot [\mathbf{g}(\mathbf{x}_t, t)\mathbf{g}(\mathbf{x}_t, t)^\top] + [\mathbf{g}(\mathbf{x}_t, t)\mathbf{g}(\mathbf{x}_t, t)^\top] \nabla_{\mathbf{x}_t} \log p_t(\mathbf{x}_t) \right] p_t(\mathbf{x}_t) \right\} \\ &= - \sum_{i=1}^N \frac{\partial}{\partial x_i} [\tilde{f}_i(\mathbf{x}_t, t)] p_t(\mathbf{x}_t) \end{aligned} \quad (27)$$

where $\tilde{\mathbf{f}}(\mathbf{x}_t, t) = \mathbf{f}(\mathbf{x}_t, t) - \frac{1}{2}\nabla \cdot [\mathbf{g}(\mathbf{x}_t, t)\mathbf{g}(\mathbf{x}_t, t)^\top] - \frac{1}{2}[\mathbf{g}(\mathbf{x}_t, t)\mathbf{g}(\mathbf{x}_t, t)^\top]\nabla_{\mathbf{x}_t} \log p_t(\mathbf{x}_t)$. With careful inspection of Eq. (27), it is equal to the Liouville equation if the diffusion term $\tilde{\mathbf{g}}(\mathbf{x}, t) = 0$ and essentially, it is the probability flow ODE where

$$\begin{aligned} d\mathbf{x}_t &= \tilde{\mathbf{f}}(\mathbf{x}_t, t)dt + \tilde{\mathbf{g}}(\mathbf{x}_t, t)d\mathbf{w}_t \\ &= \left\{ \mathbf{f}(\mathbf{x}_t, t) - \frac{1}{2}\nabla \cdot [\mathbf{g}(\mathbf{x}_t, t)\mathbf{g}(\mathbf{x}_t, t)^\top] - \frac{1}{2}[\mathbf{g}(\mathbf{x}_t, t)\mathbf{g}(\mathbf{x}_t, t)^\top]\nabla_{\mathbf{x}_t} \log p_t(\mathbf{x}_t) \right\} dt \end{aligned} \quad (28)$$

Using Eq. (28), we can derive an appropriate probability flow ODE from the forward process (1) introduced in the main text. For example, we have the following equation

$$d\mathbf{x}_t = \underbrace{\left\{ \mathbf{f}(\mathbf{x}_t, t) - \frac{1}{2}g(t)^2\nabla_{\mathbf{x}_t} \log p_t(\mathbf{x}_t) \right\} dt}_{:=\tilde{\mathbf{f}}(\mathbf{x}_t, t)} \quad (29)$$

for the toy model where $\mathbf{f}(\mathbf{x}_t, t) = 0$.

Log-likelihood. Furthermore, if we first take the logarithm of Eq. (27) where

$$\frac{\partial \log p_t(\mathbf{x}_t)}{\partial t} = \frac{1}{p_t(\mathbf{x}_t)} \frac{\partial p_t(\mathbf{x}_t)}{\partial t} = -\sum_{i=1}^N \frac{\partial \tilde{f}_i(\mathbf{x}_t, t)}{\partial x_i} = \nabla \cdot \tilde{\mathbf{f}}(\mathbf{x}_t, t) \quad (30)$$

we can compute the log-likelihood of $p_0(\mathbf{x}_0)$ using the following equation

$$\log p_0(\mathbf{x}_0) = \log p_T(\mathbf{x}_T) + \int_0^T \nabla \cdot \tilde{\mathbf{f}}(\mathbf{x}_t, t)dt \quad (31)$$

where $\nabla \cdot \tilde{\mathbf{f}}(\mathbf{x}_t, t)$ is parameterized as $\nabla \cdot \tilde{\mathbf{f}}_\theta(\mathbf{x}_t, t)$ since $s_\theta(\mathbf{x}_t, t) = \nabla_{\mathbf{x}_t} \log p_t(\mathbf{x}_t; \theta)$. Moreover, in general the term $\nabla \cdot \tilde{\mathbf{f}}_\theta(\mathbf{x}_t, t)$ is computed via the Hutchinson trace estimator [73],

$$\nabla \cdot \tilde{\mathbf{f}}_\theta(\mathbf{x}_t, t) = \mathbb{E}_{p(\epsilon)} [\epsilon^\top \nabla_{\mathbf{x}} \tilde{\mathbf{f}}_\theta(\mathbf{x}_t, t) \epsilon] \quad (32)$$

where $\nabla_{\mathbf{x}} \tilde{\mathbf{f}}_\theta(\mathbf{x}_t, t)$ denotes the Jacobian of $\tilde{\mathbf{f}}_\theta(\mathbf{x}_t, t)$ and the random variable ϵ satisfies $\mathbb{E}_{p(\epsilon)}[\epsilon] = 0$ and $\text{Cov}_{p(\epsilon)}[\epsilon] = \mathbf{I}$.

However, for the toy model in Section (3), due to its low dimensionality we find that it is possible to not utilize the Hutchinson trace estimator at all, and instead opt to compute the trace of the Jacobian without using the noise estimators — to get the actual trace of the Hessian of the energy.

D Experimental Details on the Transition Mapping

Points Selection. For the computation of Fig. (5), we follow the experiment setup of [45] and conduct a sparse search starting at data size 500 and doubling it all the way to the total data size $|\mathcal{S}|$, i.e., $K = 500, 1000, 2000, \dots, |\mathcal{S}|$. We then identified two transitional critical points, A and B ,

Dataset	Point A (Data Size)	Point B (Data Size)	Total (Data Size)
MNIST	4,000	32,000	60,000
CIFAR10	2,000	16,000	50,000
LSUN-CHURCH	2,000	16,000	126,227
FASHION-MNIST	4,000	16,000	60,000

Table 1: Table showing the critical points A and B of the memorization-generalization transition for each dataset. We use 30 linearly spaced points between A and B to finely characterize the transition plots shown in Fig. (5).

see Table (1), to conduct a more thorough search to elucidate the memorization-generalization transition. Point A indicates the initial drop in memorization while B signals the plateauing of memorization. To capture the finer details of this transition, we performed a search of 30 inclusive linearly spaced points, from point A to point B . For regions outside of the transition, using linear spacing, we sample 5 points from $|\mathcal{S}| = 2$ to point A , and another 5 points from B to the total dataset size $|\mathcal{S}|$, inclusively. In other words, we train a separate model for each selected data size and generate the corresponding evaluation and synthetic sets — keeping the same configuration for all models, see Table (3). Then, we computed the memorization, spurious, and generalization fractions using equations (13), (14), and (15). The selection process for the values δ_m and δ_s is explained below.

Dataset	δ_m	δ_s	$d(\cdot)$
CIFAR10	0.03	0.018	LPIPS
LSUN-CHURCH	0.12	0.05	LPIPS
MNIST	4.5	3.5	L_2 -distance
FASHION-MNIST	4.5	2.5	L_2 -distance

Table 2: Table displaying memorized and spurious threshold values in the computation of the transition plots in Fig. (5).

Selection of the Distance Metric. For high-dimensional datasets, CIFAR10 [63] and LSUN-CHURCH [66], we utilized LPIPS [77] with the AlexNet [78] backbone, as the function $d(\cdot, \cdot)$ for both memorization (13) and spurious (14) detection metrics. We selected this approach since it is a commonly used perceptual metric that compares the similarity between two images based on their feature representations. Moreover, it has been shown to better align with human judgment of visual similarity, making it ideal for assessing the quality and diversity of generated samples in these high-dimensional image datasets [77]. For simpler datasets like MNIST [64] and FASHION-MNIST [65], where images are single-channel and less complex, we found that L_2 -distance suffices for both memorization and spurious detection metrics.

Selection of Threshold Values δ_m and δ_s . The detection thresholds, δ_m and δ_s , were set based on the chosen distance metric $d(\cdot, \cdot)$ and visual inspection of the distance histograms for

bimodality as mentioned in Section (4) of the main text. Moreover, these thresholds were chosen to reflect the varying visual complexity and feature richness of the datasets, and their values for each dataset are shown in Table (2). For CIFAR10, we utilized the histograms obtained at $K = 7310$, which demonstrate strong bimodality shape, to tune our threshold values to minimize the number of spurious samples classified as memorized samples and vice versa, via manual inspection. For manual inspection, a general rule we followed — it is better to have more false positives in the generalized set than the memorized set since spurious samples can be seen as early-generalized samples. Thus, we observe the least-5 spurious samples and ensure that they do not resemble memorized samples. We performed the same process for memorized samples. The entire process is then repeated for the other three datasets. We utilized $K = 4896$ for LSUN-CHURCH, $K = 21379$ for MNIST, and $K = 7724$ for FASHION-MNIST to select δ_m and δ_s . For more details on the selected histograms, please refer to Figs. (4), (14), (12), and (13).

Dataset	Initial Latent	Channel Multipliers	Number of Parameters	Batch Size	Training Iterations
MNIST	128	(1, 2, 2)	24.5M	128	400,000
CIFAR10	128	(1, 2, 2, 2)	35.7M	128	500,000
CIFAR10	96	(1, 2, 2, 2)	20.1M	128	500,000
CIFAR10	64	(1, 2, 2, 2)	8.9M	128	500,000
LSUN-CHURCH	64	(1, 1, 2, 2, 4, 4)	27.4M	64	800,000
LSUN-CHURCH	96	(1, 1, 2, 2, 4, 4)	61.7M	64	800,000
LSUN-CHURCH	128	(1, 1, 2, 2, 4, 4)	109.7M	64	800,000
FASHION-MNIST	128	(1, 2, 2)	24.5M	128	400,000

Table 3: Table displaying both model and training configurations for each dataset.

Model and Training Details. For each point in our transition plots in Fig. (5), we train a DDPM-based diffusion model, where the score model is a PixelCNN++ based U-Net [79, 80]. We keep the variances, $\beta_{\min} = 10^{-4}$ and $\beta_{\max} = 2 \times 10^{-2}$, timesteps $T = 1000$, and learning rate $lr = 2 \times 10^{-4}$ for all models and datasets. Each model has 2 residual blocks [81] for each down- and up- sampling layer, while an attention block is placed at $16 \times$ resolution. We only modified the channel multipliers for each model based on the complexity of the dataset, see Table (3). If the dataset size is smaller than the specified batch size, we take the batch size to be equal to that small dataset size. For generation or inference, we use the exponential moving average (EMA) of each trained model, as delineated in [23], which was obtained with the decay value set as 0.9999 during training. Please note that we did not use random flipping in the training of our models, since we want our measurements to reflect the training data size at best as random flipping implicitly increases the number of patterns that the models see during training. However, we did use dropout (of value 0.1) for the training of CIFAR10, MNIST, and FASHION-MNIST models. Lastly, for each of the training set S_α , where $\alpha = 1, \dots, M$, they are split from the original dataset given a specific size, using the same random seed value of 3407.

Additional Experiments. Inspired by [45, 46], we extend our investigation on the memorization-generalization transition by studying the effects of varying the parameter size of the diffusion model for CIFAR10 [63] and LSUN-CHURCH [66]. The results of this experiment are recorded in Figs. (9) and (10), respectively. Specifically, we trained two additional sets of 38 diffusion models, with the initial latent dimensions of 64 and 96 respectively, and repeat the same experimental

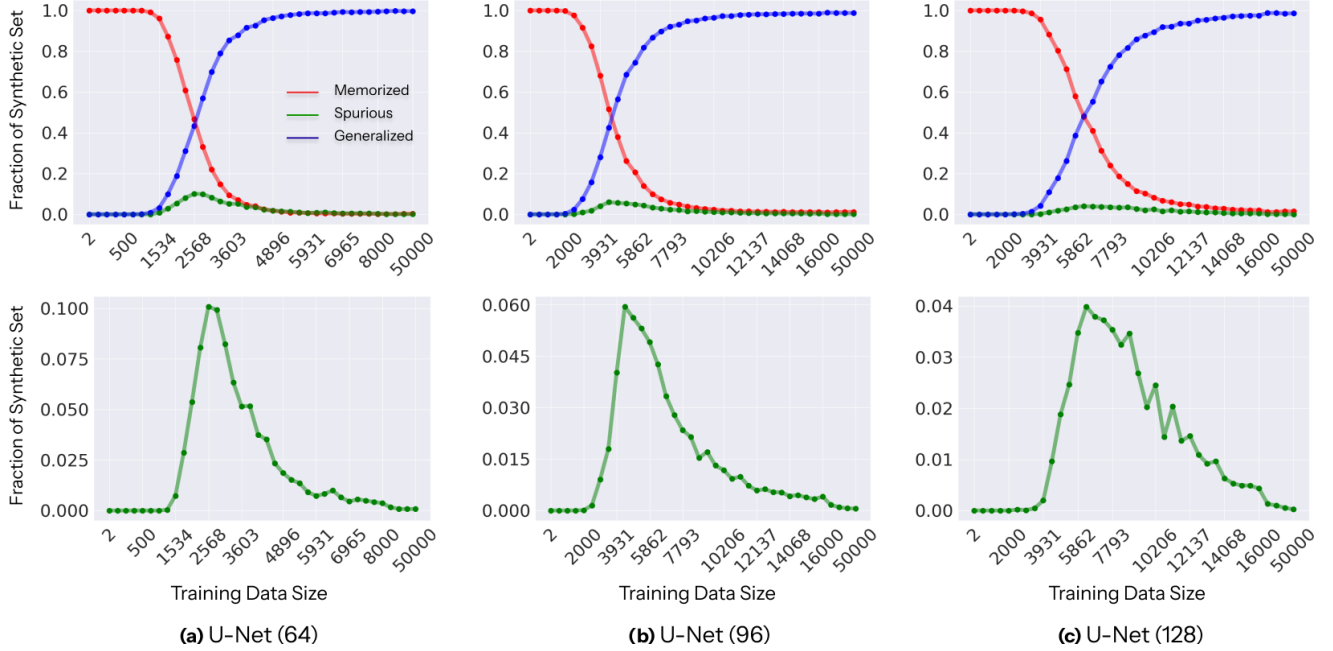


Figure 9: The fractions of **memorized**, **spurious**, and **generalized** samples in synthetic sets across different training sizes for CIFAR10 [63] and various model’s widths. As the training data size K increases, memorization decreases while the emergence of spurious patterns follows and the fraction of generalized patterns steadily increase (see **top row**). The fraction of spurious patterns rises and decreases at the boundary between the memorization and generalization phases (see **bottom row**). Additionally, with a smaller number of parameters, the memorization-generalization transition happens at an earlier stage (or smaller K), since the model has a memorization capacity. In contrast, as the model’s size increases, the transition happens at an later stage (or larger K), where it is able to memorize more training data. The numbering, e.g., 64, 96, and 128, denotes the initial latent dimension of the U-Net, see Table (3).

setup delineated above, see also Table (3).

For CIFAR10 and the U-Net (64) models, we identified the critical points, A and B , to be 500 and 8000 respectively. Meanwhile, for the U-Net (96) models, these critical points are 2000 and 16000. To select δ_m and δ_s , we followed the same process detailed above by observing the distance histograms to see where bimodality occurs with respect to the distance value, and manually inspecting the images to ensure there is a minimal amount of false positives in memorized and spurious samples. For U-Net (64) models, the threshold values δ_m and δ_s are both selected to be 0.02 based on the bimodality of the distance histograms observed at $K = 2568$ — meanwhile, for U-Net (96), the threshold values δ_m and δ_s are chosen as 0.03 and 0.02 according to distance histograms observed at $K = 3931$.

Similarly, for the LSUN-CHURCH models, we identified the critical points, A and B , to be 1000 and 8000 for the U-Net (64) models; and for the larger U-Net (128) models, 4000 and 16000 as the critical points. The threshold values, δ_m and δ_s , are both selected to be 0.04 after observing the bimodality of the distances at $K = 3413$ — meanwhile, for U-Net (128), these values are

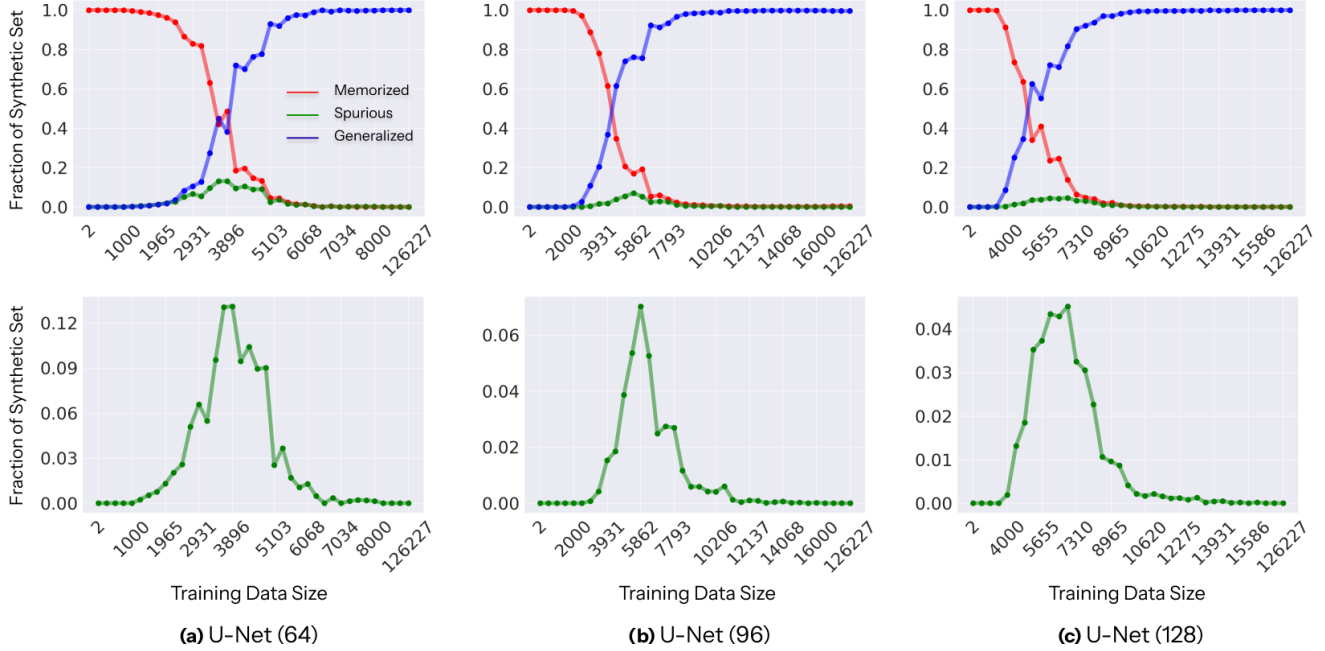


Figure 10: The fractions of **memorized**, **spurious**, and **generalized** samples in synthetic sets across different training sizes for LSUN-CHURCH [66] and various model’s widths. As the training data size K increases, memorization decreases while the emergence of spurious patterns follows and the fraction of generalized patterns steadily increase (see **top row**). The fraction of spurious patterns rises and decreases at the boundary between the memorization and generalization phases (see **bottom row**). Additionally, with a smaller number of parameters, the memorization-generalization transition happens at an earlier stage (or smaller K), since the model has a memorization capacity. In contrast, as the model’s size increases, the transition happens at an later stage (or larger K), where it is able to memorize more training data. The numbering, e.g., 64, 96, and 128, denotes the initial latent dimension of the U-Net, see Table (3).

selected to be $\delta_s = 0.04$ and $\delta_m = 0.1$ after observing the distance histograms at $K = 5241$.

With the smaller U-Net (64) models, we observe the memorization-generalization transition happens at an earlier stage with respect to the larger U-Net (128) models, where the peak of spurious samples appears at $K = 2568$ instead of $K = 5862$ for CIFAR10 and $K = 1000$ instead of $K = 4000$ for LSUN-CHURCH. Similarly, for CIFAR10 and its U-Net (96) models, the peak of spurious samples happens at an early stage of $K = 3931$ instead. Overall, these results indicate that as the parameter size of the diffusion model increases, the memorization capacity of the model is increased and thus, generalization is delayed since the model can memorize more of its training data denoted by the appearance of spurious patterns happening at a larger training data size K . In contrast, when the memorization capacity is reduced, generalization is initiated at an earlier stage (or smaller training data size) with respect to when the parameter size of the model is larger. Most importantly, the emergence of spurious patterns remains consistent despite the variations in the parameter size of the diffusion model.

Additionally, to verify the consistency of the memorization-generalization transition, we

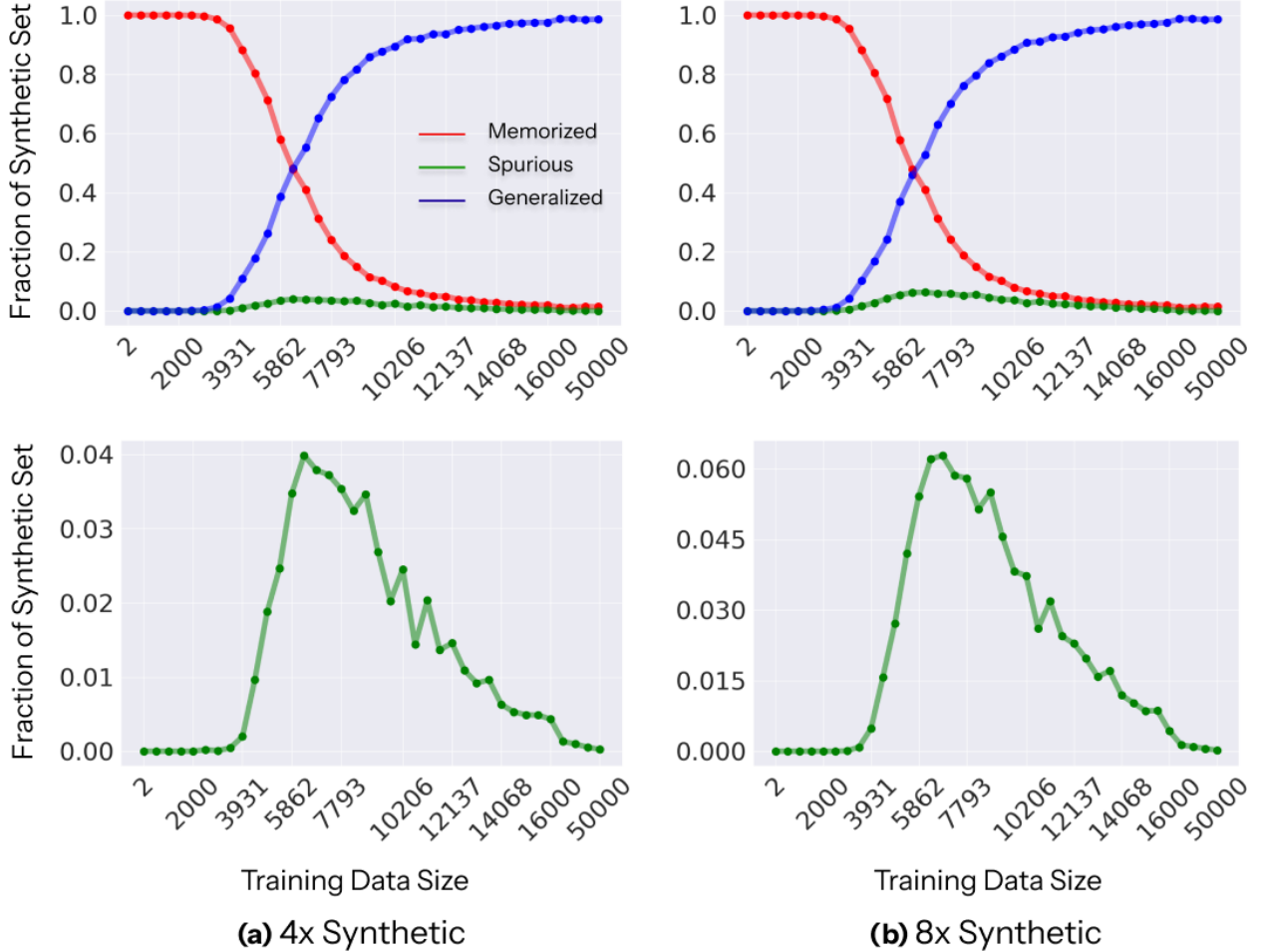


Figure 11: Memorization-Generalization transition plots for the CIFAR10 dataset. The **left** figure depicts the memorization-generalization transition computed with $4\times$ synthetic sets for various training data sizes. Meanwhile, **right** figure shows the transition computed using $8\times$ synthetic sets for the same training data sizes. With the larger synthetic sets, more spurious patterns are detected at the peak ($K = 5862$). However, the overall trend of these patterns quickly rise, during the co-existence of memorization and generalization, and fall as generalization becomes the dominant phase, is maintained. Both figures use the same memorized and spurious threshold values detailed in Table (2).

explored the influence of larger synthetic sets and recorded our results in Fig. (11). Specifically, we repeated our experiment done in Fig. (5) for CIFAR10 using $8\times$ synthetic sets — which was originally done using $4\times$ synthetic sets. Based on Fig. (11), we observe a slight increase in the fraction of spurious samples when using the larger $8\times$ synthetic sets. Specifically, at $K = 5862$, the fraction increases from 0.04 to roughly 0.06 with respect to the synthetic set size. Nonetheless, the trend of memorization-generalization, with the emergence of spurious samples, is still maintained regardless of the multiplier for the synthetic size — highlighting the consistency of the spurious phenomenon in diffusion models in relation to the training data size.

Hardware Details. The training of the models detailed in Table (3) was done using NVIDIA Tesla V100 GPUs, where a single GPU was used to train each model. Each GPU has 32GB of memory and is linked with IBM Power9 processors which clocked at 3.15 GHz. Each CIFAR10 model took roughly 18, 20, and 22 hours to train for different initial latent dimensions, e.g., 64, 96, 128, respectively. Meanwhile, each LSUN-CHURCH model requires roughly 48, 56, and 103 hours of training with respect to the model’s initial latent dimension. In contrast, FASHION-MNIST and MNIST models require approximately 17 hours to be fully trained (per model). Please note that these durations are with respect to the required training iterations for each model and their corresponding dataset detailed in Table (3). Please note that we utilized the same hardware for our experiments as well.

E Additional Visualizations of Different Sample Types Across the Transition

E.1 LSUN-CHURCH

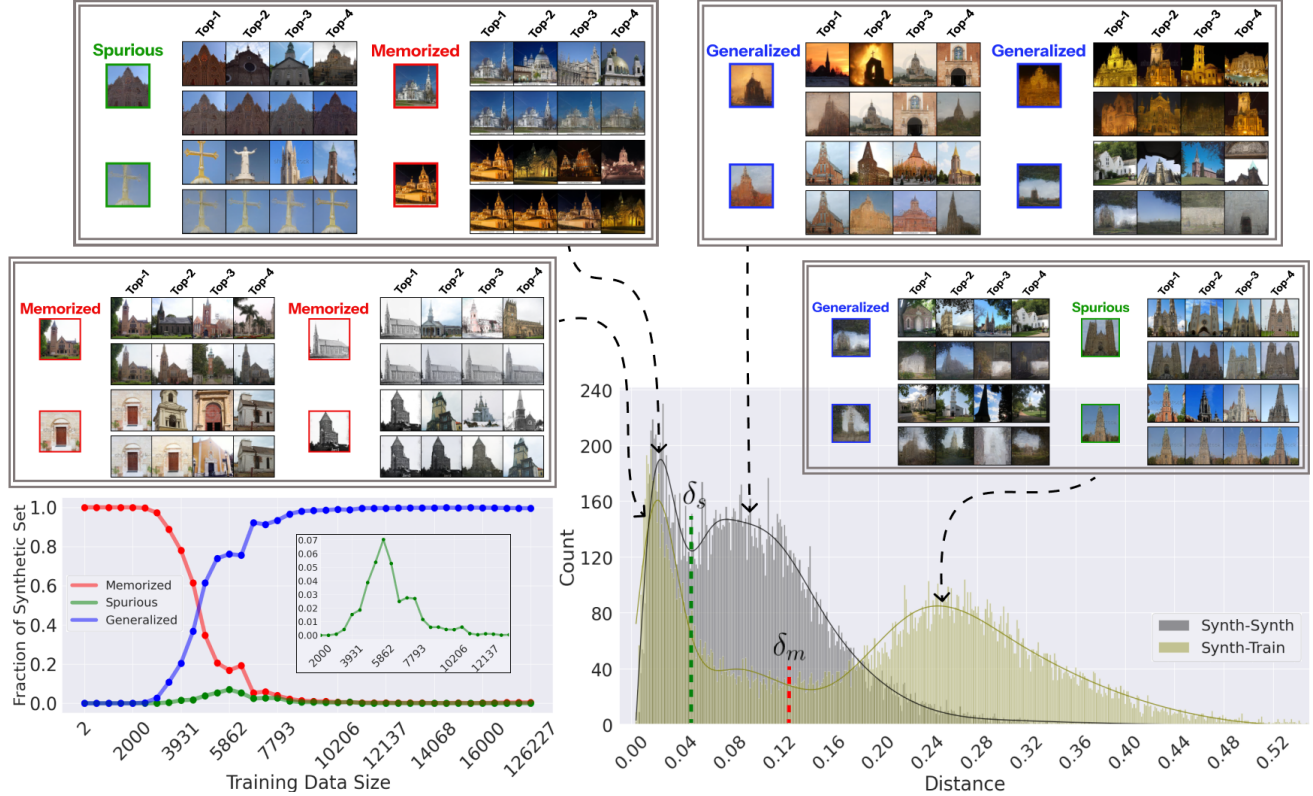


Figure 12: Different sample types across the memorization-to-generalization transition for LSUN-CHURCH [66], defined by the spurious and memorized thresholds, δ_s and δ_m . The grey histogram shows the distances between synthetic samples and their nearest neighbors from the synthetic set S' . The threshold δ_s is defined as a boundary between the two peaks. The olive histogram depicts the distances from the synthetic samples to their closest neighbor from the training set S , with threshold δ_m separating the two peaks. The threshold δ_m is chosen much stricter here such that it works well for all training dataset sizes via visual inspection. **Memorized** samples are located in the left peak of the olive histogram, below δ_m . In contrast, **generalized** and **spurious** samples appear to the right of δ_m (olive histogram). Examples of the generated samples forming each of the four peaks of the histograms are shown in the inset frames. For each generated sample **top-4** nearest neighbor images from the training set are shown in the **top row**, and top-4 nearest neighbors from the synthetic set are shown in the **bottom row**. Training set size $K = 4896$ was used in this figure (at the peak of the frequency of spurious states), but phenomena discussed are generic and largely independent of this specific value. The fraction of the memorized, spurious, and generalized samples in the pool of all generated samples is shown in the bottom left panel as a function of the training set size. The inset shows amplified spurious fraction (green curve).

E.2 FASHION-MNIST

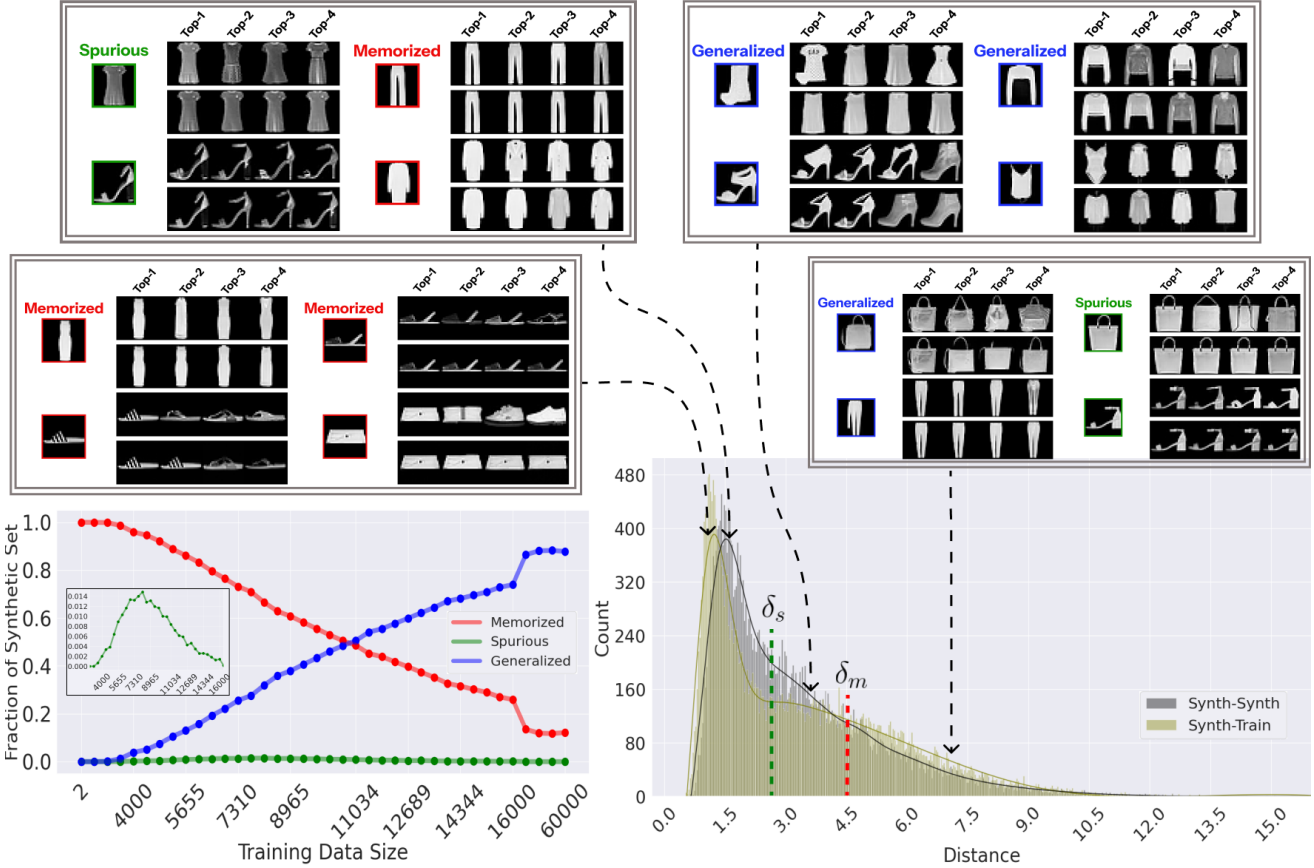


Figure 13: Different sample types across the memorization-to-generalization transition for FASHION-MNIST [65], defined by the spurious and memorized thresholds, δ_s and δ_m . The grey histogram shows the distances between synthetic samples and their nearest neighbors from the synthetic set S' . The threshold δ_s is defined as a boundary between the two peaks. The olive histogram depicts the distances from the synthetic samples to their closest neighbor from the training set S , with threshold δ_m separating the two peaks. **Memorized** samples are located in the left peak of the olive histogram, below δ_m . In contrast, **generalized** and **spurious** samples appear to the right of δ_m (olive histogram). Examples of the generated samples forming each of the four peaks of the histograms are shown in the inset frames. For each generated sample **top-4** nearest neighbor images from the training set are shown in the **top row**, and top-4 nearest neighbors from the synthetic set are shown in the **bottom row**. Training set size $K = 7724$ was used in this figure (at the peak of the frequency of spurious states), but phenomena discussed are generic and largely independent of this specific value. The fraction of the memorized, spurious, and generalized samples in the pool of all generated samples is shown in the bottom left panel as a function of the training set size. The inset shows amplified spurious fraction (green curve).

E.3 MNIST

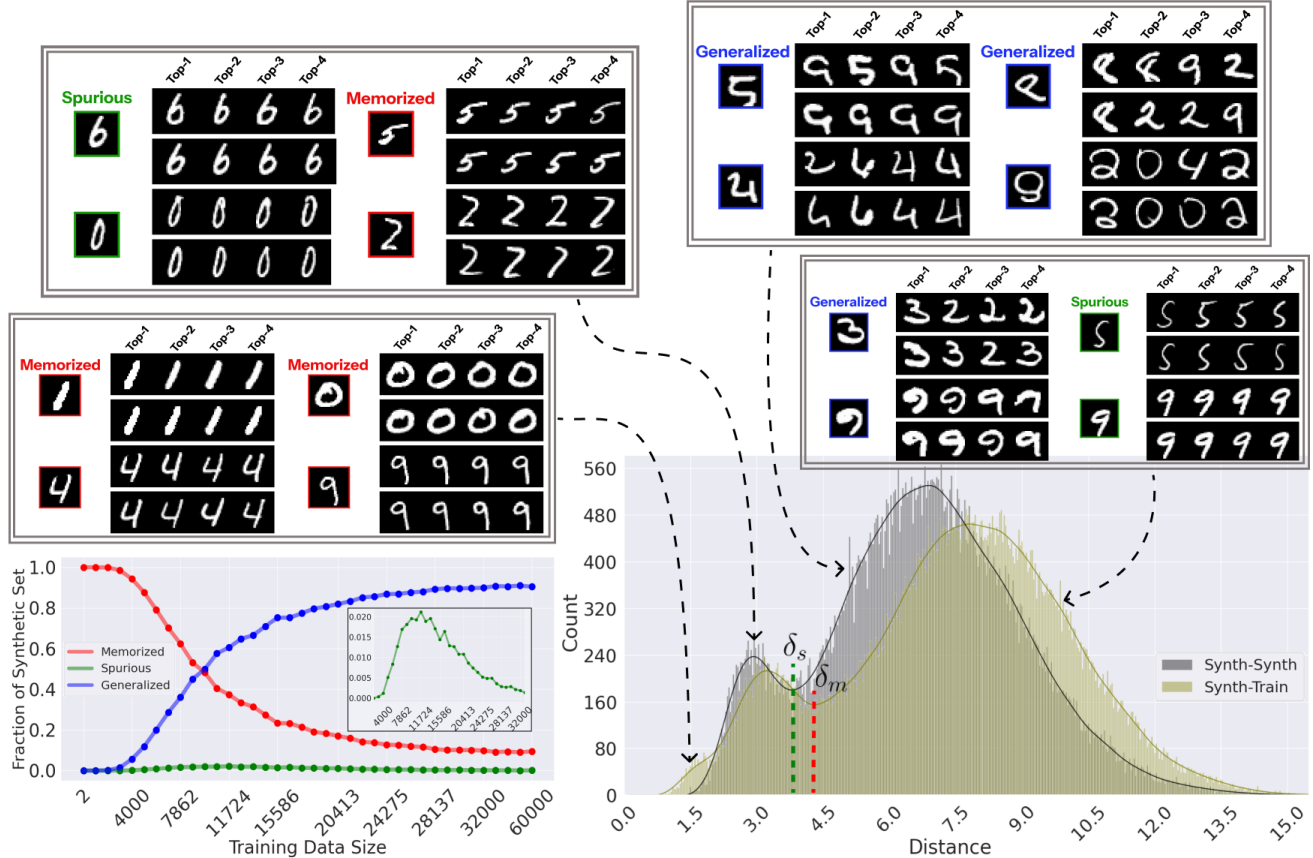


Figure 14: Different sample types across the memorization-to-generalization transition for MNIST [64], defined by the spurious and memorized thresholds, δ_s and δ_m . The grey histogram shows the distances between synthetic samples and their nearest neighbors from the synthetic set S' . The threshold δ_s is defined as a boundary between the two peaks. The olive histogram depicts the distances from the synthetic samples to their closest neighbor from the training set S , with threshold δ_m separating the two peaks. **Memorized** samples are located in the left peak of the olive histogram, below δ_m . In contrast, **generalized** and **spurious** samples appear to the right of δ_m (olive histogram). Examples of the generated samples forming each of the four peaks of the histograms are shown in the inset frames. For each generated sample **top-4** nearest neighbor images from the training set are shown in the **top row**, and top-4 nearest neighbors from the synthetic set are shown in the **bottom row**. Training set size $K = 21379$ was used in this figure, which is slightly past the peak of the frequency of spurious states. The phenomena discussed are generic and largely independent of this specific value. The fraction of the memorized, spurious, and generalized samples in the pool of all generated samples is shown in the bottom left panel as a function of the training set size. The inset shows amplified spurious fraction (green curve).

F Additional Visualizations of the Three Sample Types

F.1 Memorized Samples



Figure 15: Visualizations of additional **memorized** patterns and their **top-4** nearest neighbors for different datasets. The **top row** illustrates nearest neighbors from the training set while the **bottom row** depicts those from the synthetic set. **Memorized** samples are duplicates of the training set. During the strong memorization phase, duplicates are also found within the synthetic set. Note, even though our memorized detection metric (Eq. 13) does not utilize the synthetic set, we are showing the nearest neighbors obtained from it, for consistency.

F.2 Spurious Samples

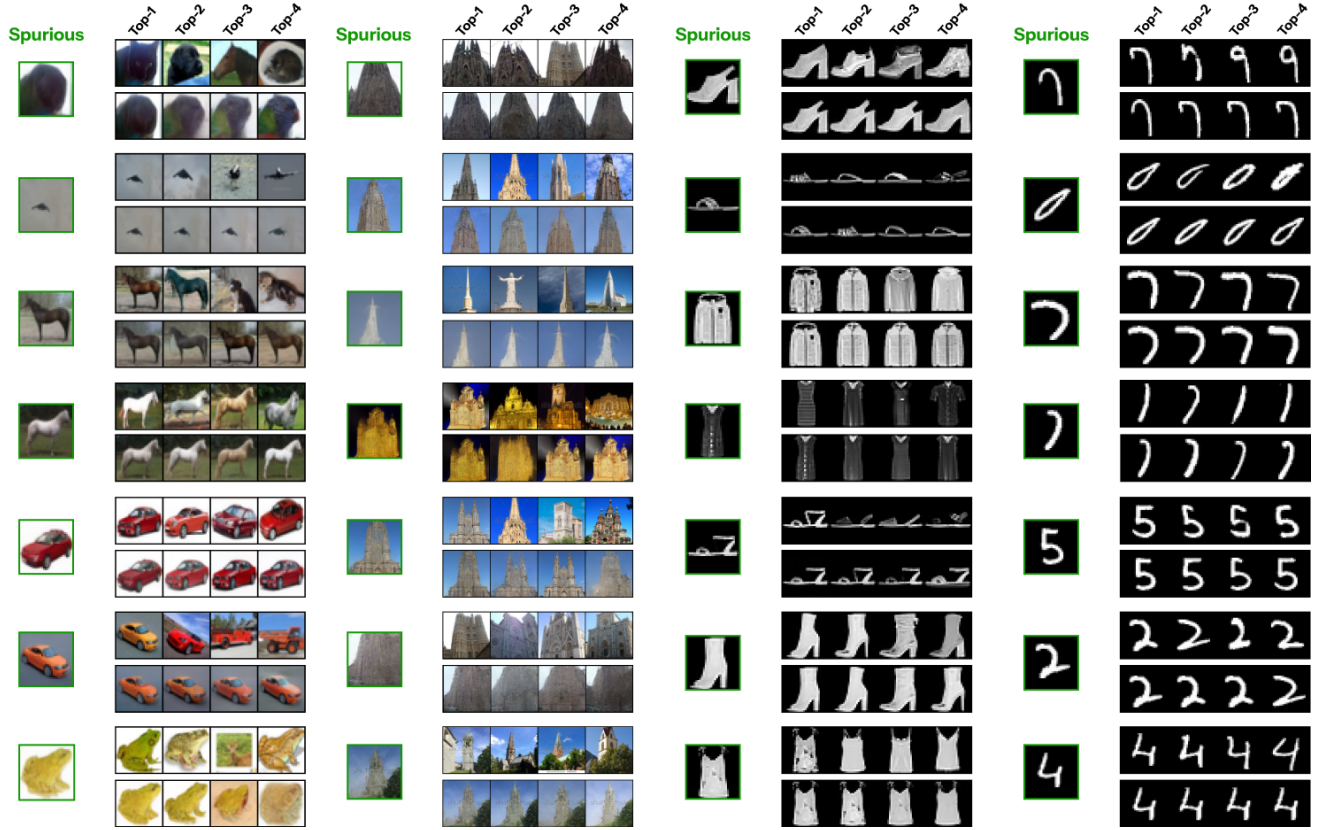


Figure 16: Visualizations of additional **spurious** patterns and their **top-4** nearest neighbors for different datasets. The **top row** depicts nearest neighbors from the training set, while the **bottom row** shows those from the synthetic set. **Spurious** patterns are demonstrated to arise from the onset of generalization where the mixing of training data points begins. Since the model’s generalization is at its infancy, duplicates of **spurious** patterns sometimes appear several times in the synthetic set S' , much like **memorized** patterns. Additionally, these samples lack the uniqueness to be considered as **generalized** samples as the model has yet to fully learn the underlying data distribution.

F.3 Generalized Samples

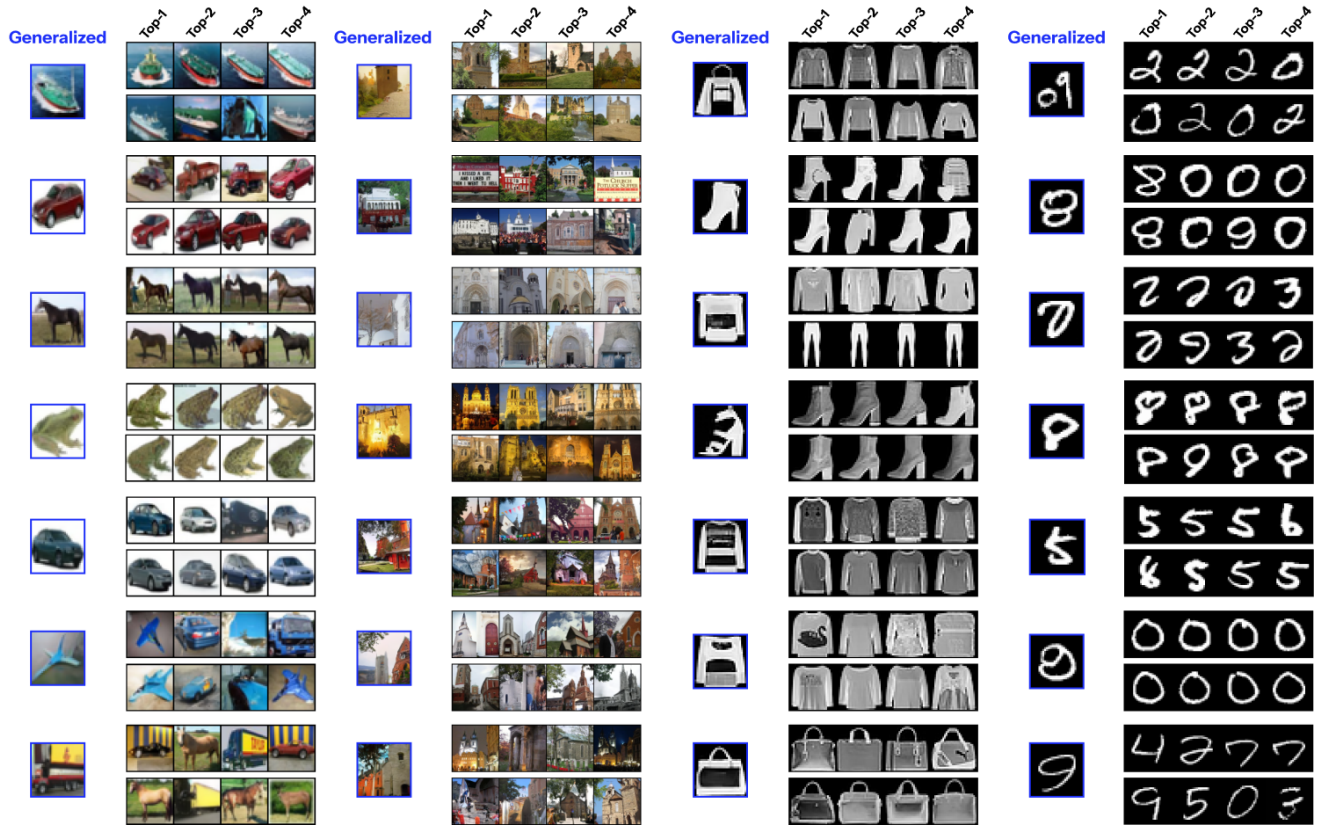


Figure 17: Visualization of **generalized** patterns and their ***top-4*** nearest neighbors for different datasets. The ***top row*** illustrates nearest neighbors from the training set while the ***bottom row*** depicts those from the synthetic set. **Generalized** samples are novel samples, which have little to no resemblance to their nearest neighbors in training and synthetic sets.

G Experimental Details on the Basin of Attraction Analysis Across the Transition

Algorithm Details. To obtain the results recorded in the above Figs. (18) and (19), we first computed the critical time t_c given an image $\mathbf{x}_0 = \mathbf{y}$. Specifically, this is done by using Algorithm (1), where t_c is obtained using the deterministic DDIM [24] sampler to denoise the perturbed version \mathbf{x}_t of \mathbf{x}_0 for each step in $t = 1, \dots, T$, given N' number of denoising steps starting backward from t to 0. To save computational time, the algorithm utilizes a stride constant s to skip over some of the timesteps $t = 1, 1+s, 1+2s, \dots, T-s-1$. For each timestep t , the variance preserving forward process is applied onto the targeted image \mathbf{x}_0 yielding \mathbf{x}_t . To account for the variations in noise, the image \mathbf{x}_0 is perturbed for M number of times at each step t .

To check whether if the critical time t_c is reached, the algorithm utilizes a distance metric d — which is LPIPS [77] equipped with the vgg-16 backbone [82] for all of the datasets — checking if a recovered image $\hat{\mathbf{x}}_0$ obtained from the DDIM sampler [24] with N' denoising steps is similar to the original pattern \mathbf{x}_0 within an error threshold $\delta_d \in (0, 1)$. Unlike the experiment on the memorization-generalization transition detailed in Section (5), we can afford to trade computational time for better accuracy in this experiment by using a larger backbone for LPIPS. Please note that the metric LPIPS is bounded between 0 (most similar) and 1 (least similar). To keep track of the critical time t_c for all perturbations, we allow it to be a vector of integers $t_c \in \mathbb{N}^M$, where M is the number of perturbations or trials for the image \mathbf{x}_0 . To ensure that t_c is correct, we have a binary stopping vector $\hat{S} \in \{0, 1\}^M$, which keeps track of whether each perturbation of \mathbf{x}_0 is no longer recoverable, such that we only update an entry of the vector t_c if and only if the corresponding entry in \hat{S} is a zero (not stopped).

Since the entire process of finding t_c is a rough search over a set of timesteps, we require a “breaking condition” for the search. In Algorithm (1), this condition is determined by the value $p \in [0, 1]$, which is a probability corresponding to the recovery probability of the image \mathbf{x}_0 with respect to its M perturbations. To compute p , we calculate the distance vector $\mathbf{d} = d(\hat{\mathbf{x}}_0, \mathbf{x}_0)$ where $\hat{\mathbf{x}}_0$ is the predicted version of \mathbf{x}_0 obtained from denoising \mathbf{x}_t . Then, we compute the recovery binary vector $\mathbf{r} \in [0, 1]^M$ by applying the indicator function onto \mathbf{d} using the threshold δ_d . Lastly, we calculate the probability value $p = \frac{1}{M} \sum_{i=1}^M \mathbf{r}_i$. If this value p is below the probability threshold δ_p , we stop the search for critical time across all trials.

Experimentation Details. For each training data size K , we used a maximum of the top 512 samples belonging to each of the sample types — e.g., training data, memorized, spurious, and generalized samples — to find their critical time t_c using Algorithm (1). Note, with the exception of the training data points, we sorted samples belonging to each set — identified via the detection metrics (13), (14) and (15) — by their distance from least to greatest. We computed the log volume using the following equation

$$V(\mathbf{x}_0, \mathbf{x}_{t_c}) = \frac{\pi^{\frac{N}{2}}}{\Gamma(\frac{N}{2} + 1)} R(\mathbf{x}_0, \mathbf{x}_{t_c})^N \quad (33)$$

where $\Gamma(\cdot)$ is the Euler’s gamma function [83] and N is the dimensionality of the image. The radius $R(\mathbf{x}_0, \mathbf{x}_{t_c})$ is the Euclidean norm of the difference between the original image \mathbf{x}_0 and its

recoverable perturbation \mathbf{x}_{t_c} . For Figs. (6), (18), and (19), we plotted the average log-volume value per each training data size K . Meanwhile, for Algorithm (1), we fixed the stopping probability δ_p as 0.8, the number of perturbations M as 20, the DDIM steps N' as 10 and the stride constant s as 10 for all datasets. At some training data size K , in which there are very few samples in either memorized, spurious or generalized set, we opted to not include the statistics of such a set, partly due to its large variance. We remove the statistics of such a set if the number of its samples is less than 0.1% of its corresponding synthetic set for a training data size K .

For CIFAR10 and LSUN-CHURCH, we utilized the threshold δ_d as 0.03 and 0.12 respectively. We kept these threshold values similar to the memorized threshold values δ_m detailed in Table (2), since they have proven to be effective at separating the memorized samples from non-memorized ones in the previous experiment. However, since it is difficult to select the threshold value for the L_2 -distance metric — because the range of the metric is between 0 and ∞ — we opted to use LPIPS to experiment with MNIST and FASHION-MNIST using the same threshold $\delta_d = 0.1$ for both. To find this optimal threshold value, we selected three data sizes, where each belongs to one of the three phases: memorization, spurious, or generalization. We then observed which of the several threshold values, starting from 0.01 to 0.15 with the increment of 0.01, reflects best of the performance given by LPIPS using vgg-16 [82] as its backbone. Specifically, we evaluated these thresholds using $K \in \{4000, 11724, 60000\}$ for MNIST, and $K \in \{4000, 8965, 60000\}$ for FASHION-MNIST. We simply perform Algorithm (1) for those three data sizes on a small batch of 32 samples for the three sample types, and manually check whether the recovered samples (using the obtained critical time t_c to denoise from) are similar to the original images and if this observation is consistent across those three data sizes.

G.1 Algorithm for Computing the Critical Time

Algorithm 1: Compute Critical Time t_c for a single pattern \mathbf{y}

```

1  Inputs
2    Pattern  $\mathbf{y}$ 
3    Score model  $s_\theta$ 
4    DDIM sampler  $\Phi$ 
5    Error threshold  $\delta_d$ 
6    Distance metric  $d$ 
7    Denoising steps  $N'$ 
8    Total diffusion time  $T$ 
9    Time stride  $s$ 
10   Number of trials  $M$ 
11   Probability threshold  $\delta_p$ 
12   Cumulative variances  $\bar{\alpha}$ 
13   Variances  $\beta$ 

14 Compute  $t_c$ 
15    $\mathbf{x}_0 \leftarrow \text{duplicate}(\mathbf{y}, M)$            // Duplicate pattern  $\mathbf{y}$  for  $M$  times
16    $t_c \leftarrow \mathbf{0}$                            // Initialize critical time tracker
17    $\hat{S} \leftarrow \mathbf{0}$                          // Track trials that have stopped

18   for  $t = 1, 1 + s, 1 + 2s, \dots, T - s - 1$  do
19      $\mathbf{z}_t \sim \mathcal{N}(0, \mathbf{I})$                    // Sample noise
20      $\mathbf{x}_t \leftarrow \sqrt{\bar{\alpha}_t} \mathbf{x}_0 + \sqrt{1 - \bar{\alpha}_t} \mathbf{z}_t$  // Forward diffusion
21      $\hat{\mathbf{x}}_0 \leftarrow \Phi(s_\theta, \mathbf{x}_t, t, \bar{\alpha}, \beta, N')$  // DDIM denoising
22      $\mathbf{d} \leftarrow d(\hat{\mathbf{x}}_0, \mathbf{x}_0)$            // Compute distance per trial

23      $\mathbf{r}_i \leftarrow \begin{cases} 1 & \text{if } \mathbf{d}_i \leq \delta_d \\ 0 & \text{otherwise} \end{cases} \text{ for } i = 1, \dots, M$  // Binary recovery vector
24      $p \leftarrow \frac{1}{M} \sum_{i=1}^M \mathbf{r}_i$            // Recovery probability

25     if  $p < \delta_p$  then
26       return  $t_c$ 
27     else
28        $\hat{S} \leftarrow \text{update-stop}(\hat{S}, \mathbf{r})$ 
29        $t_c \leftarrow \text{update-time}(t, t_c, \hat{S})$ 

30 Output
31   Critical time  $t_c \in \mathbb{N}^M$ 

```

G.2 The Basin of Attraction Across the Transition for All Datasets

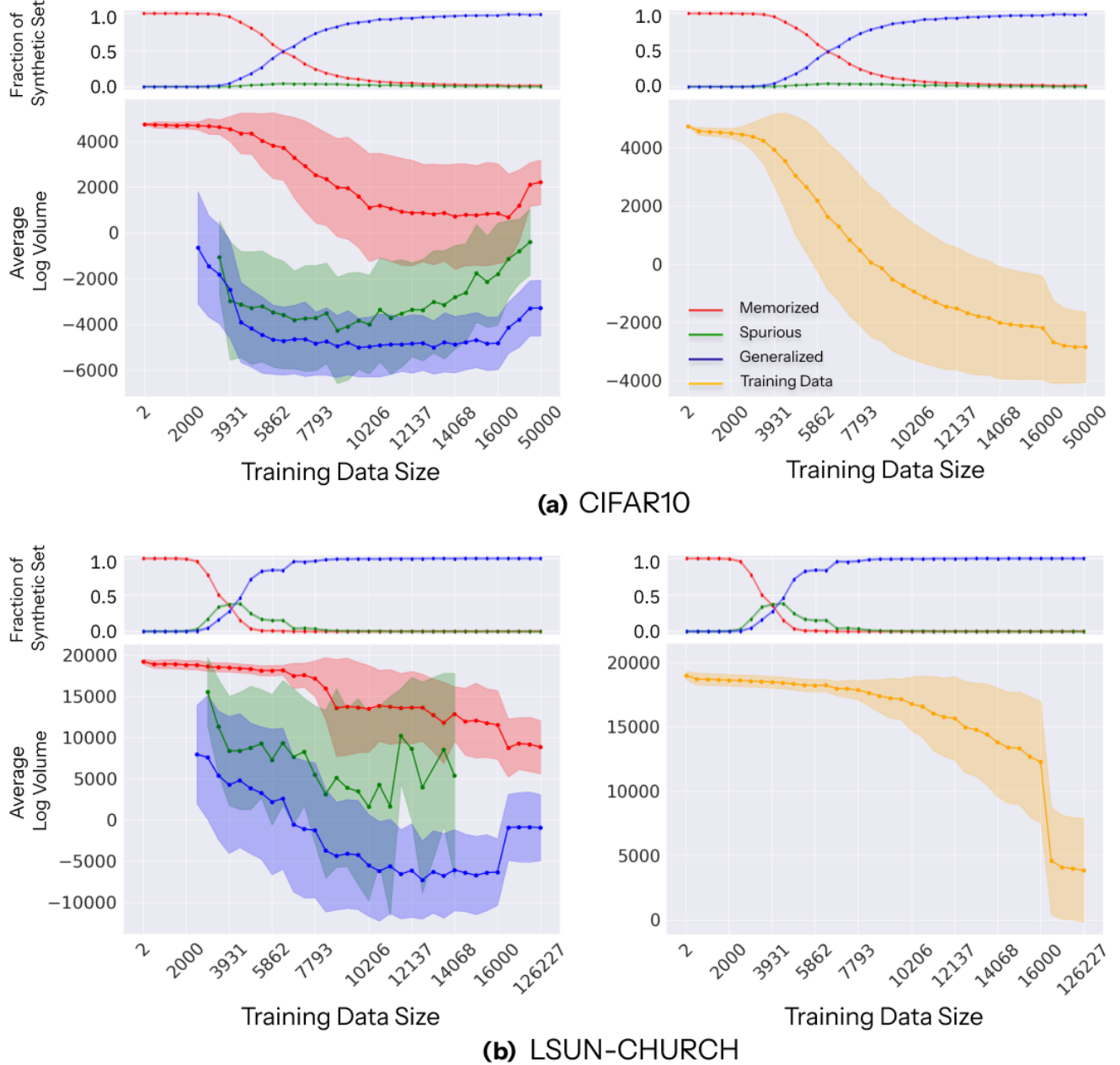
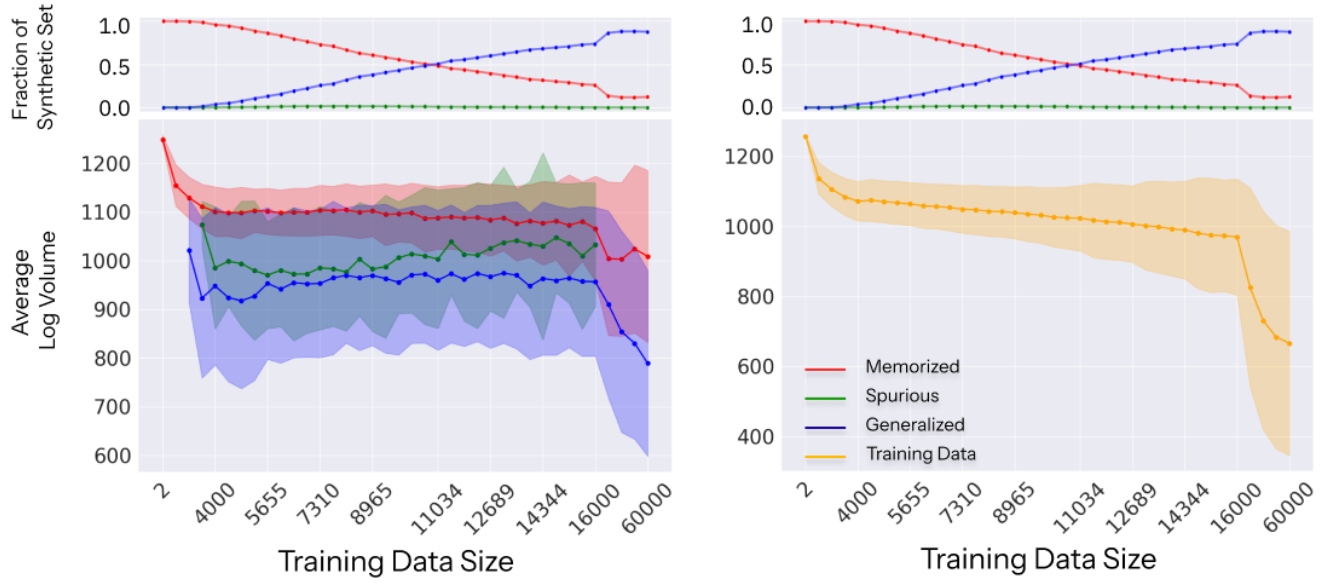
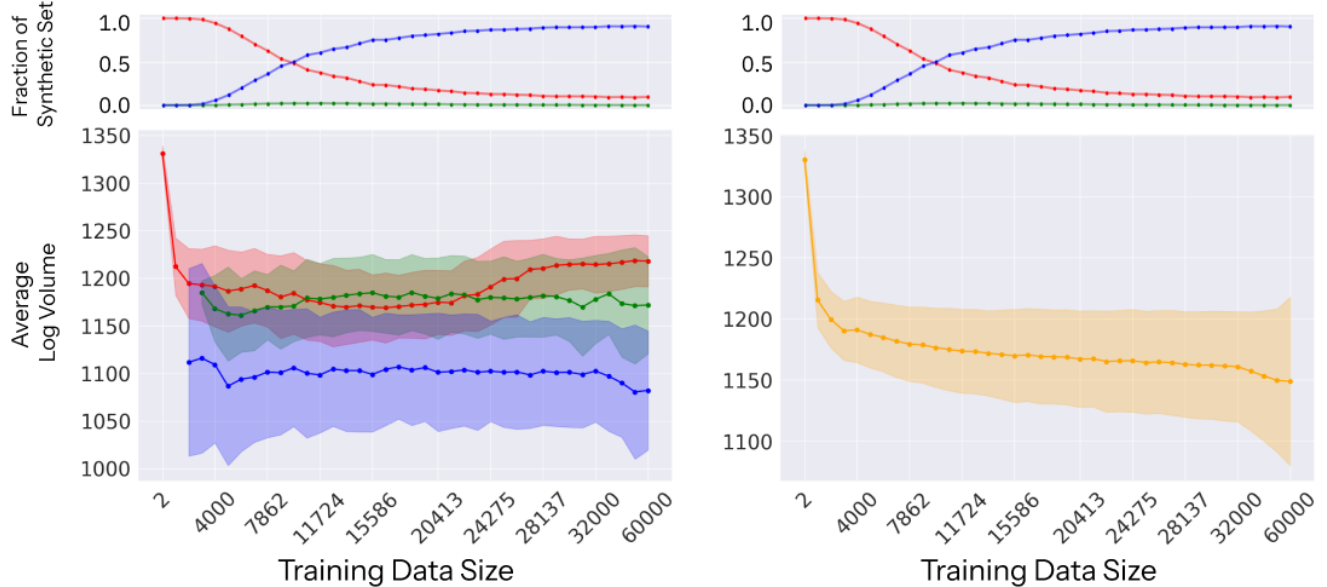


Figure 18: Average log-volume of the hyperspheric basin of attraction of different sample types as the training data size K grows, in CIFAR10 and LSUN-CHURCH computed using Eq. (33) with up to 512 samples per type. When fewer than 512 samples are available, all points are used. The log-volume of training samples and the transition plot from Fig. (5) are included to confirm the shrinking basins of attraction in diffusion models. Variations in the critical time t_c during the transition, which affect the radius R , lead to distinct log-volume trends across sample types, see the recorded critical times in Fig. (20). Shaded regions indicate standard deviation of the log-volume.



(c) FASHION-MNIST



(d) MNIST

Figure 19: Average log-volume of the hyperspheric basin of attraction of different sample types as the training data size K grows, in FASHION-MNIST and MNIST, computed using Eq. (33) with up to 512 samples per type. When fewer than 512 samples are available, all points are used. The log-volume of training samples and the transition plot from Fig. (5) are included to confirm the shrinking basins of attraction in diffusion models. Variations in critical time t_c and radius R lead to distinct log-volume trends across sample types, see the recorded critical times in Fig. (21). Shaded regions indicate standard deviation of the log-volume.

G.3 Average Critical Time Across The Transition

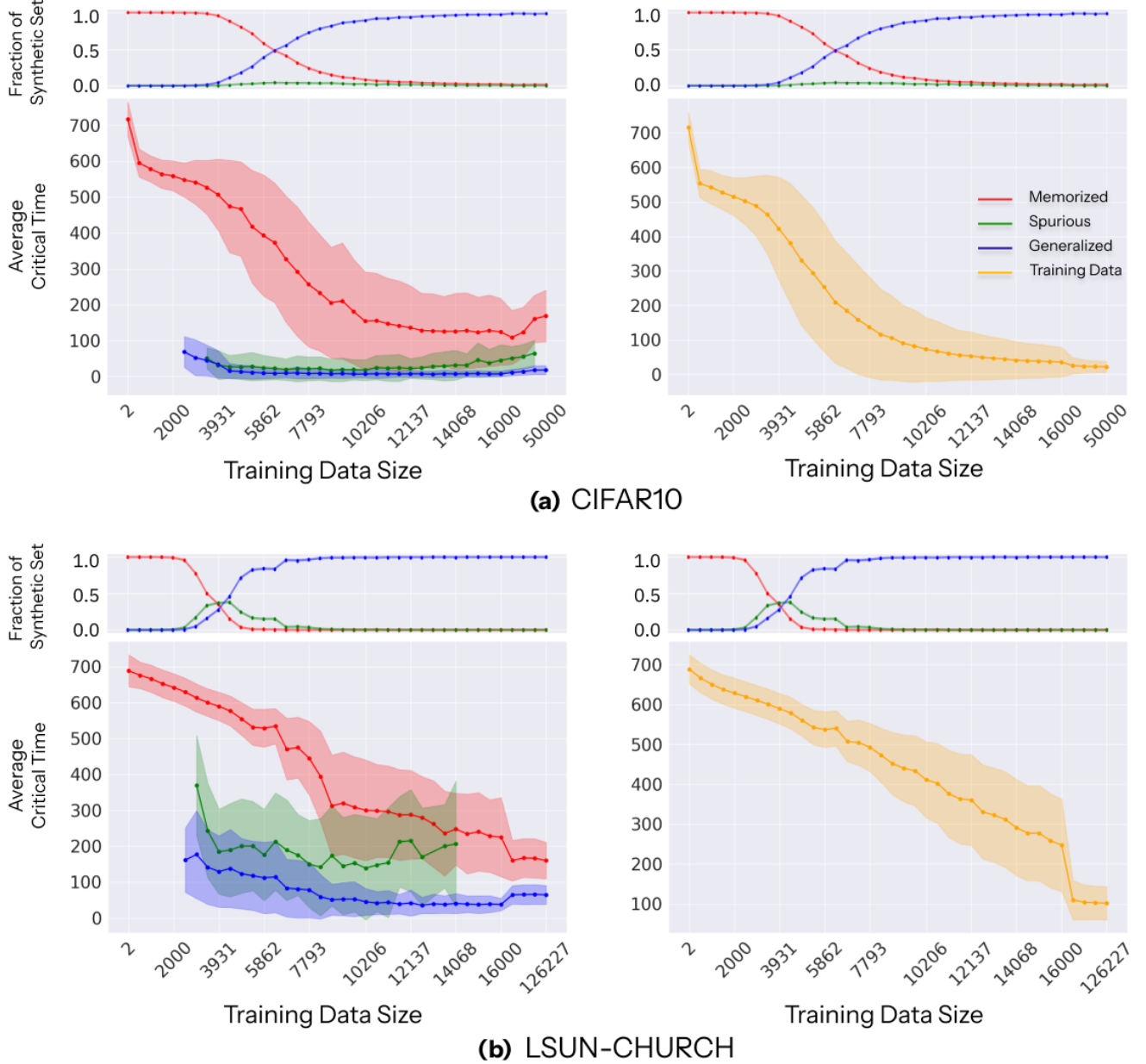


Figure 20: Average critical time, obtained using Algorithm (1), with a maximum of 512 samples across the memorization-generalization transition for each sample type in CIFAR10 and LSUN-CHURCH. The average critical times for the training data samples at each training data size K are included to illustrate the overall decrease in the time and also the amount of perturbation in which the diffusion model can effectively recover the original sample within some error. Each sample type exhibits a distinctive critical time at each training data size K . The shaded region (or the error bars) shown here is the standard deviation computed from all of the critical times at each K with respect to each type of samples. The transition plot of each dataset is shown here to visually guide where the memorization-generalization transition occurs.

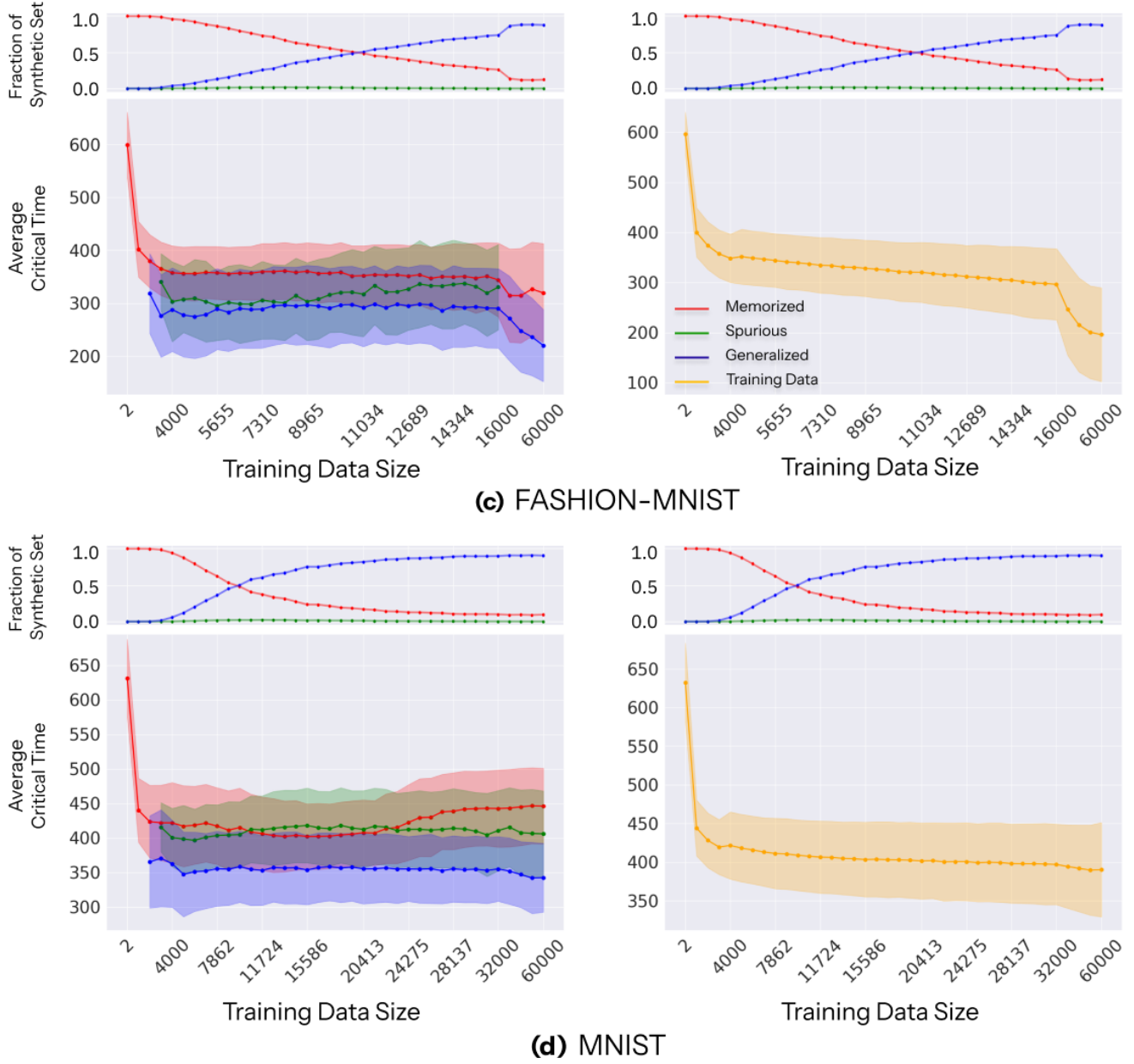


Figure 21: Average critical time, obtained using Algorithm (1), with a maximum of 512 samples across the memorization-generalization transition for each sample type in FASHION-MNIST and MNIST. The average critical times for the training data samples at each training data size K are included to illustrate the overall decrease in the time and also the amount of perturbation in which the diffusion model can effectively recover the original sample within some error. Each sample type exhibits a distinctive critical time at each training data size K . The shaded region (or the error bars) shown here is the standard deviation computed from all of the critical times at each K with respect to each type of samples. The transition plot of each dataset is shown here to visually guide where the memorization-generalization transition occurs.

G.4 Visual Demonstration of the Shrinkage of the Basins of Attraction

Experiment Details. For Fig. (7), we randomly selected a subset of training images that are shared across all 38 diffusion models, each trained with a different training set size. To determine an appropriate timestep $t \approx t_c$, we referred to Fig. (20), which plots the average critical time t_c as a function of training data size K . From this plot, we identified a plateau point in the memorization fraction curve, occurring around $K = 3931$, and selected $t_c \approx 450$ for CIFAR10. Using the timestep starting at 450, each image was perturbed via the forward process and then denoised using the DDIM sampler [24] with 25 steps across all models (starting backward from the indicated timestep). We manually examined the denoised outputs across training sizes to assess whether the resulting generations effectively illustrate the shrinkage of the basin of attraction. If the output appeared overly memorized (or too close to the original), we increased the timestep by increments of 10 and repeated the process to obtain a more illustrative transition. Lastly, in the case of LSUN-CHURCH, we selected the initial timestep to be 550 accordingly to Fig. (20).

H Additional Details on the Relative Energy Computation and its Experimentation

In this section, we provide details on the formulation of the relative energy done by [38] and an overview on the experiment done in Section (7) of the main text.

Relative Energy Formulation. Consider the SDE for the reverse process in Eq. (2) of the main text

$$d\mathbf{x}_t = [\mathbf{f}(\mathbf{x}_t, t) - g(t)^2 \nabla_{\mathbf{x}_t} \log p_t(\mathbf{x}_t)] dt + g(t) d\bar{\mathbf{w}}_t \quad (34)$$

We can re-express the above equation with the potential function $u(x, t)$

$$-\nabla_{\mathbf{x}_t} u(\mathbf{x}_t, t) = \mathbf{f}(\mathbf{x}_t, t) - g(t)^2 \nabla_{\mathbf{x}_t} \log p_t(\mathbf{x}_t) \quad (35)$$

by using the drift term. By moving the minus sign and taking the integration of Eq. (35) with respect to \mathbf{x}_t , we have

$$u(\mathbf{x}_t, t) = g(t)^2 \log p_t(\mathbf{x}_t) + \int_{\mathbf{x}_t}^0 f(\mathbf{z}, t) d\mathbf{z} \quad (36)$$

which is the potential function $u(\mathbf{x}_t, t)$ of the generative process. Substituting this potential function (36) into the reverse SDE (2), we have the following generative process

$$d\mathbf{x}_t = -\nabla_{\mathbf{x}_t} u(\mathbf{x}_t, t) dt + g(t) d\bar{\mathbf{w}}_t \quad (37)$$

For our experimental setting, where we use the DDPM [23] setting, we have the following variance preserving forward SDE

$$d\mathbf{x}_t = -\frac{1}{2} \beta(t) \mathbf{x}_t dt + \sqrt{\beta(t)} d\mathbf{w}_t \quad (38)$$

and the corresponding reverse (or generative) process SDE

$$d\mathbf{x}_t = \left[-\frac{1}{2} \beta(t) \mathbf{x}_t - \beta(t) \nabla_{\mathbf{x}_t} \log p_t(\mathbf{x}_t) \right] dt + \sqrt{\beta(t)} d\bar{\mathbf{w}}_t \quad (39)$$

With Eq. (37), we have

$$d\mathbf{x}_t = -\nabla_{\mathbf{x}_t} u(\mathbf{x}_t, t) dt + \sqrt{\beta(t)} d\bar{\mathbf{w}}_t \quad (40)$$

and by using Eq. (35), the potential for our experimental setting equates to

$$\begin{aligned} u(\mathbf{x}_t, t) &= g(t)^2 \log p_t(\mathbf{x}_t) + \int_{\mathbf{x}_t}^0 f(\mathbf{z}, t) d\mathbf{z} \\ &= \beta(t) \log p_t(\mathbf{x}_t) + \frac{1}{2} \beta(t) \int_{\mathbf{x}_t}^0 \mathbf{z}_t d\mathbf{z} \\ &= \beta(t) \log p_t(\mathbf{x}_t) - \frac{1}{4} \beta(t) \mathbf{x}_t^2 \end{aligned} \quad (41)$$

Assume we have two images, $\mathbf{x}_1(t)$ and $\mathbf{x}_2(t)$, where \mathbf{x}_1 is a target image and $\mathbf{x}_2(t)$ is a reference image at time t . Since we are interested in the energy of unperturbed images, let $\mathbf{x}_1 = \mathbf{x}_1(0)$ and $\mathbf{x}_2 = \mathbf{x}_2(0)$. As discussed in [38], the N -dimensional potential of a diffusion model can be projected down into 1-dimension via a generative trajectory between \mathbf{x}_1 and \mathbf{x}_2 . We can obtain such a trajectory via circular interpolation between \mathbf{x}_1 and \mathbf{x}_2 following

$$\tilde{\mathbf{x}}(\alpha) = \cos(\alpha)\mathbf{x}_1 + \sin(\alpha)\mathbf{x}_2 \quad (42)$$

and compute the relative potential (up to a constant) as a function of α by using

$$\tilde{u}(\alpha) = u(\tilde{\mathbf{x}}(\alpha)) = \int_0^{\pi/2} \nabla u(\tilde{\mathbf{x}}(\alpha)) \cdot \mathbf{v} \, d\alpha \quad (43)$$

where $\mathbf{v} = -\sin(\alpha)\mathbf{x}_1 + \cos(\alpha)\mathbf{x}_2$. See Fig. (22) for a visualization of this circular interpolation between two samples. For discrete times, we instead estimate the relative energy as

$$\tilde{u}(\bar{\alpha}_L) \approx \sum_{i=1}^L \nabla u(\tilde{\mathbf{x}}(\bar{\alpha}_i)) \cdot \mathbf{v} \Delta\alpha \quad (44)$$

given that $\bar{\alpha} = \{0, \dots, \frac{\pi}{2}\}$ and the potential $u(\cdot)$ is obtained from the above Eq. (41). **Experimentation Details.** In our experimentation of Section (7), we utilized a maximum of the top 2048 samples for each of three sample types (i.e., memorized, spurious, and generalized sets), and the training data set corresponding at each training data size K . Note, with the exception of the training data set, the samples in the three sets are sorted from least to greatest, based on their distance corresponding to their respective detection metric, e.g., Eq. (13), (14) or (15). We computed the relative energy of each set following Algorithm (2), which is strictly following the formulations detailed above. Note, we randomly selected and utilized an image from the entire training set as part of the relative energy calculation.

To define the average relative energy gap, let $\tilde{u}_{\text{target}} \in \mathbb{R}^M$ be a set of M relative potentials computed from using either a memorized, spurious, or generalized set and following Eq. (44). Please note that M is capped at 2048 samples. Since at some training data size K , certain sample type sets might not have less than 2048 samples. For such cases, we use the entirety of that set to compute the relative energy of its samples. Meanwhile, let $\tilde{u}_{\text{data}} \in \mathbb{R}^{M'}$ be the set of relative potentials computed from the training dataset at size K , where $M' = 2048$ for $K \geq 2048$. The average relative energy gap is defined as

$$\Delta(\tilde{u}_{\text{target}}, \tilde{u}_{\text{data}}) = \frac{1}{M} \sum_{i=1}^M (\tilde{u}_{\text{target}})_i - \frac{1}{M'} \sum_{j=1}^{M'} (\tilde{u}_{\text{data}})_j = \mu(\tilde{u}_{\text{target}}) - \mu(\tilde{u}_{\text{data}}) \quad (45)$$

Using Eq. (45), we computed the average relative energy gap and recorded our results in Figs. (8) and (23). The shaded regions reported in these figures represent the standard deviations computed from using $\tilde{u}_{\text{target}}$, and the average relative energy gap as the mean value. Since at some training data size K , there might be very few samples in one of the three sets, we opted not to include the relative energy gap of such sets, partly due to their large variance. Similar to

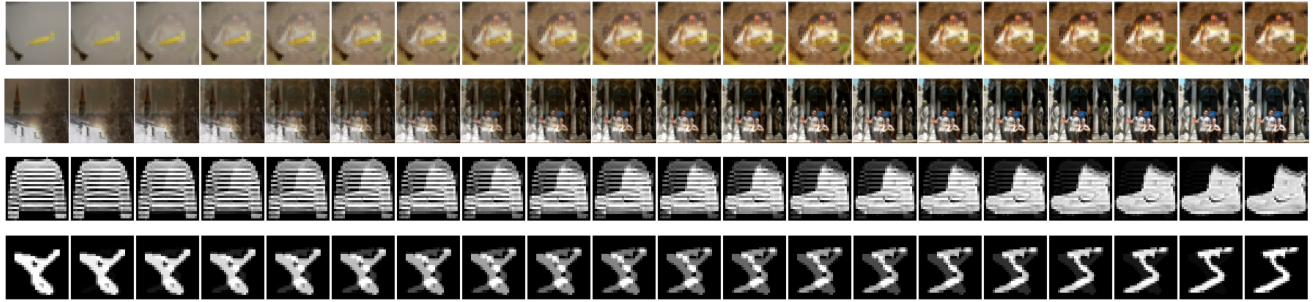


Figure 22: Circular interpolation of a target image \mathbf{x}_1 and a reference image \mathbf{x}_2 over $\alpha \in \{0, \dots, \frac{\pi}{2}\}$ for different datasets.

the basin of attraction experiment, we determine whether a set is too small if the number of its samples is less than 0.1% of its corresponding synthetic set. Finally, for our interpolation values $\bar{\alpha} = \{0, \dots, \frac{\pi}{2}\}$ detailed in Algorithm (2) and used in Eq. (44), we generate 20 points starting from 0 to $\frac{\pi}{2}$ using linear spacing.

Moreover, since the relative energy computation requires a reference image, we studied the effects of having different reference images on the relative energy gap in Figs. (24), (25), (26), and (27). Overall, there is a slight difference in the values of the relative energy gap across the memorization-generalization transition for all datasets. However, the general trend is still maintained. Specifically, the gap for memorized samples is initially close to zero and quickly diverges as the training data size K increases. Spurious samples' relative potential resembles that of the training data samples during the intermediate phase of the memorization-generalization phase. However, the potential of spurious states quickly diverges as the later stages of generalization are initiated and consequently, where the gap between generalized and training data samples' relative energy significantly decreases.

H.1 Algorithm for Computing Relative Energy

Algorithm 2: Compute the Discretized Relative Energy between a target \mathbf{x}_1 and a reference \mathbf{x}_2

```

1 Inputs
2   Target pattern  $\mathbf{x}_1 \in \mathbb{R}^N$ 
3   Reference pattern  $\mathbf{x}_2 \in \mathbb{R}^N$ 
4   Score model  $s_\theta$ 
5   Interpolation values  $\bar{\alpha}$ 
6   Initial variance  $\beta_0$ 

7 Assumption:  $\mathbf{x}_1$  and  $\mathbf{x}_2$  are samples at  $t = 0$ 
8

9 Compute  $\tilde{u}(\bar{\alpha}_L)$ 
10   $\tilde{u}(\bar{\alpha}_L) \leftarrow 0$ 
11   $\bar{\alpha} \leftarrow \{0, \dots, \frac{\pi}{2}\}$  // Linear Spacing from 0 to  $\frac{\pi}{2}$ 
12   $\Delta\alpha \leftarrow \bar{\alpha}_1 - \bar{\alpha}_0$ 
13  for  $\alpha \in \bar{\alpha}$  do
14     $\tilde{\mathbf{x}} \leftarrow \cos(\alpha)\mathbf{x}_1 + \sin(\alpha)\mathbf{x}_2$ 
15     $\tilde{\mathbf{v}} \leftarrow -\sin(\alpha)\mathbf{x}_1 + \cos(\alpha)\mathbf{x}_2$ 
16     $\nabla_{\tilde{\mathbf{x}}} \log p_0(\tilde{\mathbf{x}}) \leftarrow -s_\theta(\tilde{\mathbf{x}}, 0)/\sqrt{\beta_0}$ 
17     $\nabla_{\tilde{\mathbf{x}}} u(\tilde{\mathbf{x}}) \cdot \mathbf{v} \Delta\alpha \leftarrow \left( -\frac{1}{2}\beta_0 \tilde{\mathbf{x}} - \beta_0 \nabla_{\tilde{\mathbf{x}}} \log p_0(\tilde{\mathbf{x}}) \right) \cdot \mathbf{v} \Delta\alpha$  // See Eq. (39)
18
19     $\tilde{u}(\alpha) \leftarrow \sum_{j=1}^N \left( \nabla_{\tilde{\mathbf{x}}} u(\tilde{\mathbf{x}}) \cdot \mathbf{v} \Delta\alpha \right)_j$  // Sum over  $N$  pixels
20
21     $\tilde{u}(\bar{\alpha}_L) \leftarrow \tilde{u}(\bar{\alpha}_L) + \tilde{u}(\alpha)$  // See Eq. (44)
22 Output
23  Relative energy  $\tilde{u}(\bar{\alpha}_L)$ 

```

H.2 Average Relative Energy Gap of Sample Types for All Datasets

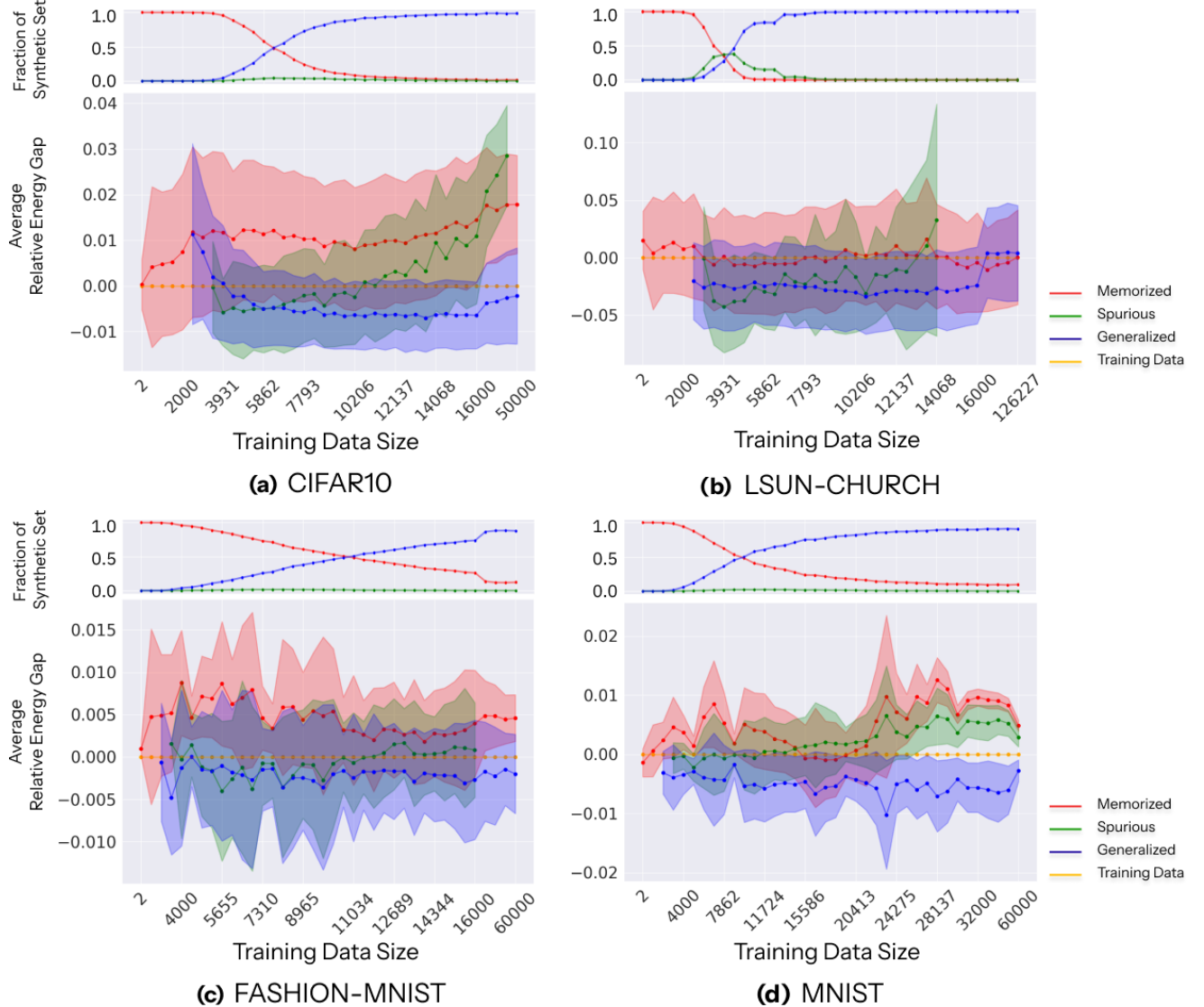
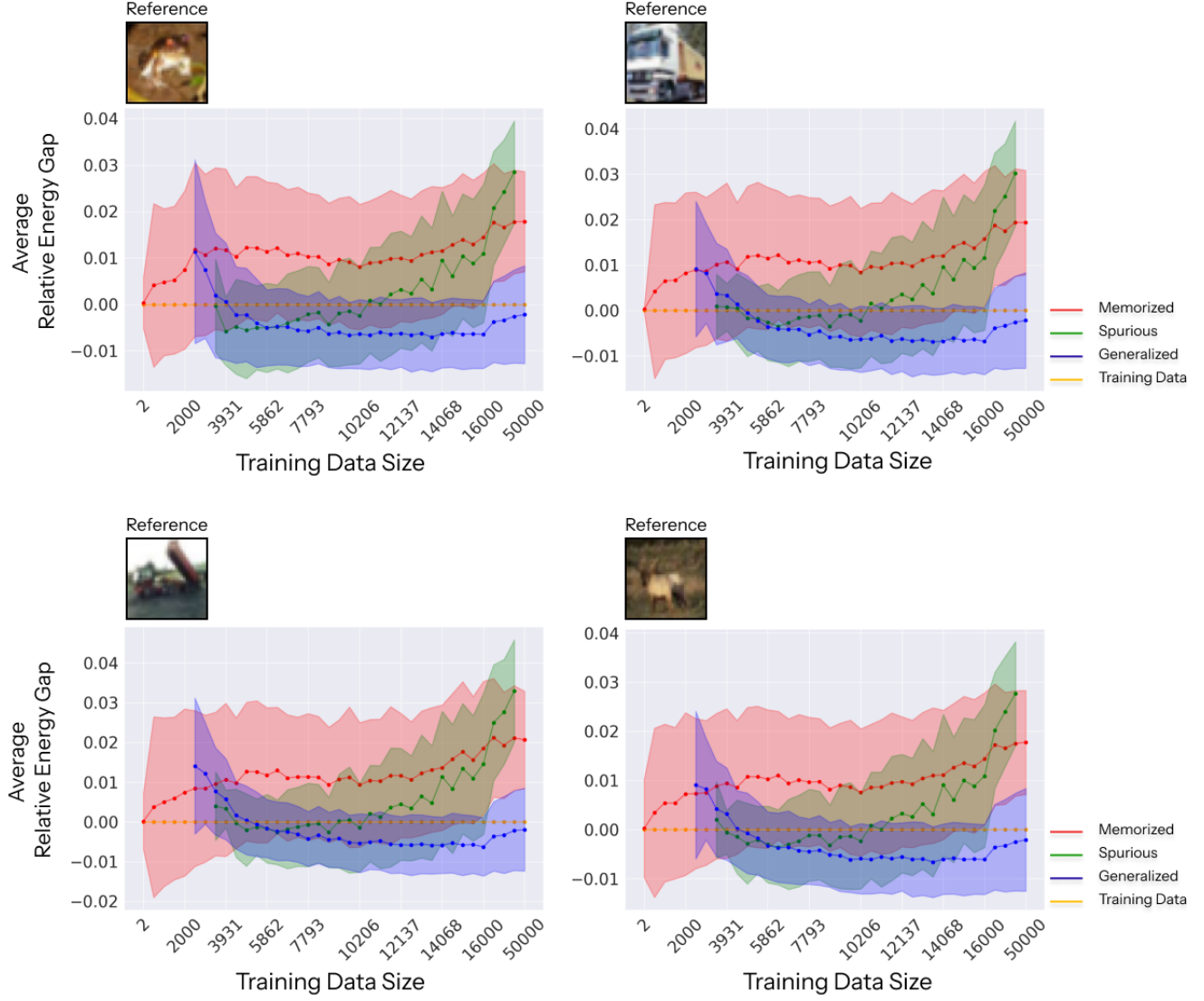


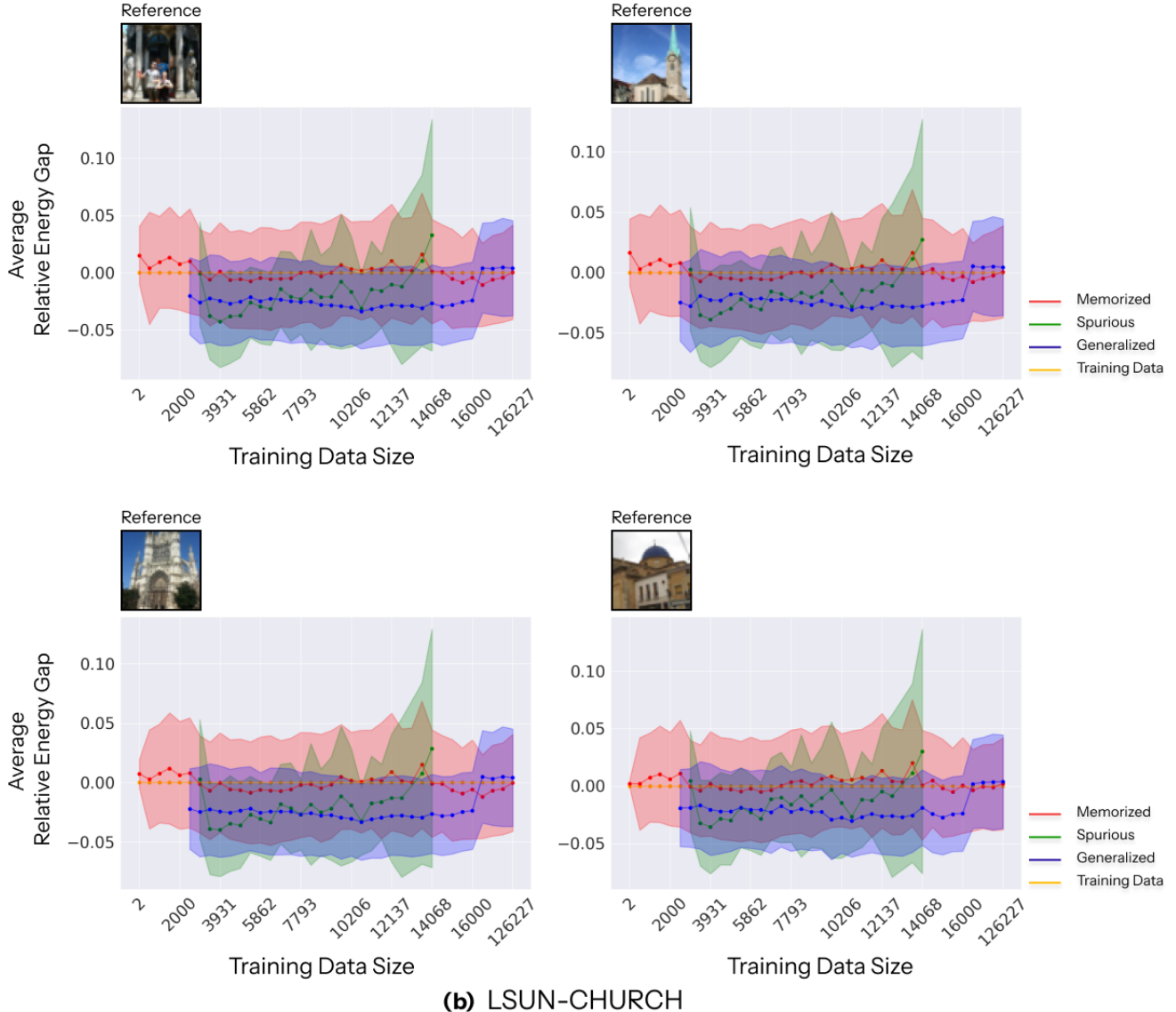
Figure 23: Average energy gap of each sample type and the training samples for the four datasets as the training data size K grows, computed using Eq. (44). Gaps are measured relative to training samples, whose energy is set to zero since there is no gap to itself. A maximum of 2048 samples per type is used at each K , or the full set is used instead if there are fewer than 2048 points. Shaded regions show standard deviation of the gap values. With the exception of LSUN-CHURCH, the relative energy of the memorized samples matches that of the training data samples at $K = 2$, but quickly diverges as K increases. Similarly, spurious samples' relative potential resembles that of the training data samples during the intermediate phase of the memorization-generalization phase. However, the potential quickly diverges as the later stages of generalization are initiated and consequently, the gap between generalized and training data samples' relative energy significantly decreases.

H.3 Average Relative Energy Gap using Different Reference Images for All Datasets



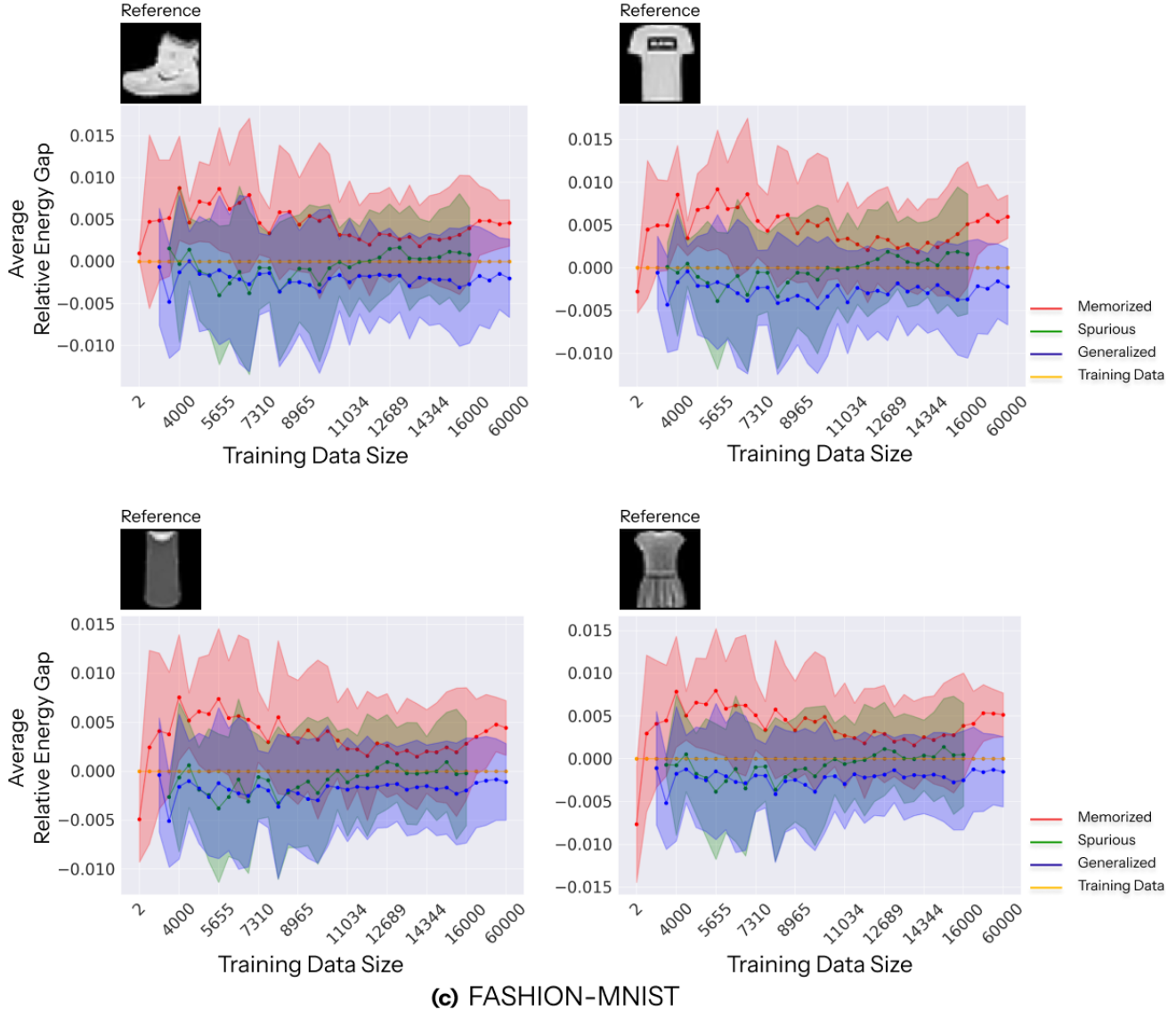
(a) CIFAR10

Figure 24: Average energy gap of each sample type and the training samples of CIFAR10 as the training data size K grows, computed using Eq. (44) and four different reference images. Gaps are measured relative to training samples, whose energy is set to zero since there is no gap to itself. A maximum of 2048 samples per type is used at each K , or the full set is used instead if there are fewer than 2048 points. Shaded regions show standard deviation of the gap values. The relative energy gap values are slightly different for distinct reference images but the general trend remains. The gap for memorized samples is initially close to zero and quickly diverges as the training data size K increases. Similarly, spurious samples' relative potential resembles that of the training data samples during the intermediate phase of the memorization-generalization phase. However, the potential quickly diverges as the later stages of generalization are initiated and consequently, the gap between generalized and training data samples' relative energy significantly decreases.



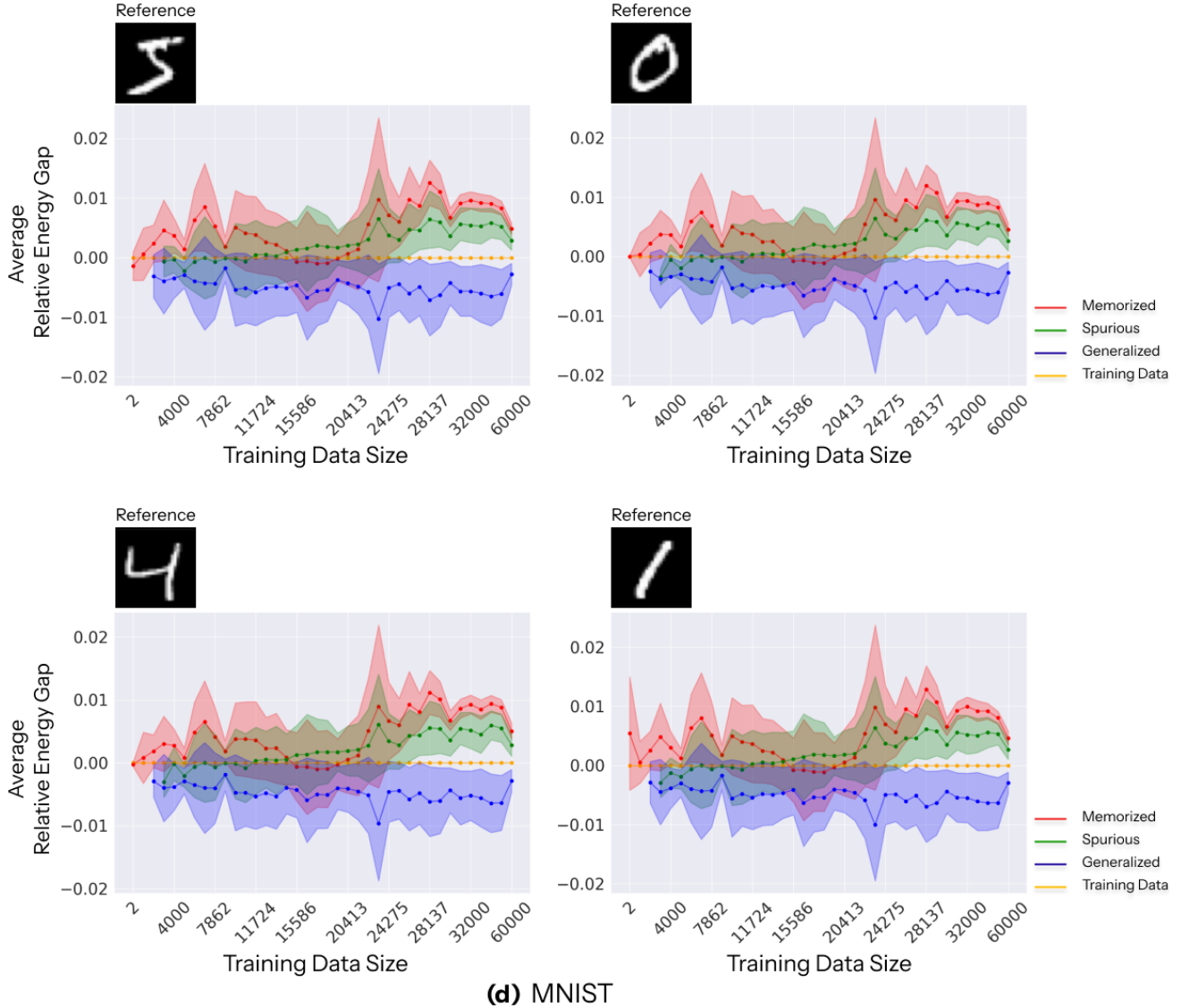
(b) LSUN-CHURCH

Figure 25: Average energy gap of each sample type and the training samples of LSUN-CHURCH as the training data size K grows, computed using Eq. (44) and four different reference images. Gaps are measured relative to training samples, whose energy is set to zero since there is no gap to itself. A maximum of 2048 samples per type is used at each K , or the full set is used instead if there are fewer than 2048 points. Shaded regions show standard deviation of the gap values. The relative energy gap values are slightly different for distinct reference images but the general trend remains. The gap for memorized samples is initially close to zero and quickly diverges as the training data size K increases. Similarly, spurious samples' relative potential resembles that of the training data samples during the intermediate phase of the memorization-generalization phase. However, the potential quickly diverges as the later stages of generalization are initiated and consequently, the gap between generalized and training data samples' relative energy significantly decreases.



(c) FASHION-MNIST

Figure 26: Average energy gap of each sample type and the training samples of FASHION-MNIST as the training data size K grows, computed using Eq. (44) and four different reference images. Gaps are measured relative to training samples, whose energy is set to zero since there is no gap to itself. A maximum of 2048 samples per type is used at each K , or the full set is used instead if there are fewer than 2048 points. Shaded regions show standard deviation of the gap values. The relative energy gap values are slightly different for distinct reference images but the general trend remains. The gap for memorized samples is initially close to zero (for three of the reference images) and quickly diverges as the training data size K increases. Similarly, spurious samples' relative potential resembles that of the training data samples during the intermediate phase of the memorization-generalization phase. However, the potential quickly diverges as the later stages of generalization are initiated and consequently, the gap between generalized and training data samples' relative energy significantly decreases.



(d) MNIST

Figure 27: Average energy gap of each sample type and the training samples of MNIST as the training data size K grows, computed using Eq. (44) and four different reference images. Gaps are measured relative to training samples, whose energy is set to zero since there is no gap to itself. A maximum of 2048 samples per type is used at each K , or the full set is used instead if there are fewer than 2048 points. Shaded regions show standard deviation of the gap values. The relative energy gap values are slightly different for distinct reference images but the general trend remains. The gap for memorized samples is initially close to zero (for three of the reference images) and quickly diverges as the training data size K increases. Similarly, spurious samples' relative potential resembles that of the training data samples during the intermediate phase of the memorization-generalization phase. However, the potential quickly diverges as the later stages of generalization are initiated and consequently, the gap between generalized and training data samples' relative energy significantly decreases.